SANDIA REPORT

SAND2008-6968
Unlimited Release
Printed November 2008

Doppler electron velocimetry: Notes on creating a practical tool

Phillip L. Reu
Contributions by Tom Milster

Prepared by
Sandia National Laboratories
Albuquerque, New Mexico 87185 and Livermore, California 94550

Sandia is a multiprogram laboratory operated by Sandia Corporation,
a Lockheed Martin Company, for the United States Department of Energy's
National Nuclear Security Administration under Contract DE-AC04-94AL85000.

Approved for public release; further dissemination unlimited.

Issued by Sandia National Laboratories, operated for the United States Department of Energy by Sandia Corporation.

NOTICE: This report was prepared as an account of work sponsored by an agency of the United States Government. Neither the United States Government, nor any agency thereof, nor any of their employees, nor any of their contractors, subcontractors, or their employees, make any warranty, express or implied, or assume any legal liability or responsibility for the accuracy, completeness, or usefulness of any information, apparatus, product, or process disclosed, or represent that its use would not infringe privately owned rights. Reference herein to any specific commercial product, process, or service by trade name, trademark, manufacturer, or otherwise, does not necessarily constitute or imply its endorsement, recommendation, or favoring by the United States Government, any agency thereof, or any of their contractors or subcontractors. The views and opinions expressed herein do not necessarily state or reflect those of the United States Government, any agency thereof, or any of their contractors.

Printed in the United States of America. This report has been reproduced directly from the best available copy.

Available to DOE and DOE contractors from
U.S. Department of Energy
Office of Scientific and Technical Information
P.O. Box 62
Oak Ridge, TN 37831

Telephone: (865) 576-8401
Facsimile: (865) 576-5728
E-Mail: reports@adonis.osti.gov
Online ordering: http://www.osti.gov/bridge

Available to the public from
U.S. Department of Commerce
National Technical Information Service
5285 Port Royal Rd.
Springfield, VA 22161

Telephone: (800) 553-6847
Facsimile: (703) 605-6900
E-Mail: orders@ntis.fedworld.gov
Online order: http://www.ntis.gov/help/ordermethods.asp?loc=7-4-0#online

SAND2008-6968
Unlimited Release
Printed November 2008

Doppler Electron Velocimetry: Notes on creating a Practical Tool

Phillip L. Reu
Tom Milster, University of Arizona
01534 – Mechanical Environments
Sandia National Laboratories
P.O. Box 5800
Albuquerque, New Mexico 87185-MS1139

Abstract

The Doppler electron velocimeter (DEV) has been shown to be theoretically possible [1, 2]. This report attempts to answer the next logical question: Is it a practical instrument? The answer hinges upon whether enough electrons are available to create a time-varying Doppler current to be measured by a detector with enough sensitivity and bandwidth. The answer to both of these questions is a qualified yes. A target Doppler frequency of 1 MHz was set as a minimum rate of interest. At this target a theoretical beam current signal-to-noise ratio of 25-to-1 is shown for existing electron holography equipment. A detector is also demonstrated with a bandwidth of 1-MHz at a current of 10 pA. Additionally, a Linnik-type interferometer that would increase the available beam current is shown that would offer a more flexible arrangement for Doppler electron measurements over the traditional biprism.

ACKNOWLEDGMENTS

I owe a deep debt of gratitude to Bruce Hansche for his mentoring and support throughout the development of this project. He contributed the work used for the optical-analogy Linnik microscope work.

For the electron multiplier development, I would like to thank Bonnie McKenzie for her expert help with the scanning electron microscope, in what can only be called a non-standard configuration. Similarly, I would like to thank Joe Michael for his support and a number of fruitful discussions on how best to conduct the experiments.

It is safe to say that the electronics and successful implementation of the electron multiplier would not have happened without the work of Jerry Stoker. Without his incredible expertise and insight into the amplification of the signal I am confident the results would have not been nearly as good as they were.

Tom Milster of the University of Arizona is also appreciated for a number of lively and enlightening conversations which ultimately lead to his suggestion of a possible means of arranging a Mach-Zehnder interferometer in an electron microscope.

CONTENTS

1. Introduction ... 11
   1.1. Doppler electron background ... 11
      1.1.1. de Broglie waves ... 11
      1.1.2. Interference of electrons ... 12
      1.1.3. Möllenstadt electron biprism ... 13
   1.2 Applications for DEV ... 14

2. Theory ... 15
   2.1. Analysis of Basic Electron Holography ... 15
   2.2. Introduction to Coherence ... 17
   2.3. Spatial Coherence ... 19
   2.4. Temporal Coherence ... 24
   2.5. Application of Theory to Inelastic Energy Loss ... 25

3. Linnik Microscope experiments ... 27
   3.1. Introduction to the Linnik microscope ... 27
   3.2. Improving beam current via imaging the source ... 29
   3.3. Single point Linnik Doppler measurements ... 30
   3.4. Conclusions ... 33

4. Electron detection experimental work ... 35
   4.1. TEM experimental failures and the move to the SEM ... 36
   4.2. SEM Testing of the Faraday Cup ... 37
   4.3. Electron Multiplier Testing in the SEM ... 39
      4.3.1 Electron Multiplier and Amplification Circuitry ... 39
      4.3.2 Electron Multiplier Results ... 43
   4.4. Evaluation of the EM as a High-Rate Beam Current Detector. ... 46

5. Potential applications for the DEV ... 47
   5.2 Applications Introduction ... 47
   5.2. Mechanical Motion ... 47
   5.3. Varying electric fields ... 48
   5.4. Varying magnetic fields ... 48

6. Conclusions ... 49
   6.1. Possible DEV Configurations and Applications ... 49

7. References ... 51
   A.1 Imaging in each path ... 53
   A.2 The coherence function and fringe visibility ... 54
   A.3 Incoherent illumination pupil (Critical illumination) ... 56
   A.4 Kohler illumination ... 59

Distribution ... 62

FIGURES

Figure 1. Point source interference model. 13
Figure 2. Möllenstadt biprism. 14
Figure 3. Schematic of biprism holography setup [4] 15
Figure 4. Simplified ray diagram of basic electron holography. The specimen is not shown. 16
Figure 5. Young's double hole interferometer showing coherence effects on fringe contrast. 19
Figure 6. A second point source of electron waves (B) is added at location (x_s,0). The net result is a fringe shift Δx_d for the B fringes, where $\Delta x_d = x_s$. The resulting current density is the sum of individual fringe patterns 21
Figure 7. Visibility $\mathcal{V}$ as a function of x_s for the geometry of Figure 6. 21
Figure 8. Point source ray diagram of Linnik Microscope 28
Figure 9. Collimated LED looking at a small mirror. A slight tilt is added to the object to create the fringes. Field-of-view is approximately 330 μm. 29
Figure 10. Linnik microscope set-up in a critical illumination case with the source imaged at the pupil and again on the reference and object legs. The wavefront splitting mirror is shown in the center. 31
Figure 11. Photo of wave-front splitting half-silvered mirror. 32
Figure 12. Diagram and resulting amplitudes at the detector for a wave-front splitting arrangement. 32
Figure 13. Focal spot of split-beam interferometer, with beams in and out of phase 33
Figure 14. Schematic of an Everhardt-Thornley secondary electron detector (http://commons.wikimedia.org/wiki/Category:Secondary_electron_detector). 35
Figure 15. Schematic of a solid state detector. (http://commons.wikimedia.org/wiki/Image:Solid_state_electron_detector.JPG) 36
Figure 16. Electron multiplier and schematic. 36
Figure 17. Electron microscope used for experiments. 37
Figure 18. Commercial Faraday cup with 50-μm hole. 38
Figure 19. Faraday wire shown in the shielding cup in the SEM. 39
Figure 20. Faraday scope trace (Yellow) and ET detector trace (Blue). 39
Figure 21. Shielded EM used in the experiments. 40
Figure 22. Electron multiplier mounted in SEM chamber. 40
Figure 23. SEM Microscope showing electrical wiring. 41
Figure 24. Gain curve for the DeTech electron multiplier (from literature sent with the multiplier). 42
Figure 25. Amplifier schematic. 42
Figure 26. Scan rate versus repetition rate. 43
Figure 27. Rise time for different scan rates. 44
Figure 28. Rise-time experiment showing a 2.5 MHz bandwidth 45
Figure 29. Typical signal response showing the noise levels at different beam currents. 46
Figure 30. STEM Holography. (a) Conceptual diagram; and (b) Experimental setup. (From Leuthner *et al*. 1989.) 49
Figure 31. Conceptual arrangement of a Mach-Zehnder-like STEM DEV device. 50

TABLES

Table 1. Sample electron wavelengths and electron microscope accelerating potential. 12
Table 2. Typical electron source brightness and beam currents. 17
Table 3. Doppler signal level for different Linnik configurations. 29
Table 4. Electron multiplier SNR for different beam currents. 45
Table 5. Dynamic rates for a 1-MHz sampling capability 48

NOMENCLATURE

A	Electron source or source current per unite area or electromagnetic field vector
a	Distance from source to biprsim
α	Source angle
B	Magnetic field or Beam brightness
b	Distance from biprism to viewing plane
β	Angle between object wave and reference wave
c	speed of light
dB	decibel
DOE	Department of Energy
d	Specimen thickness
∇	Del operator
Δ	Gradient function
E	Electron energy or Electric field
e	Electron charge
f_D	Doppler frequency
$\mathbf{F}^{-1}$	Fourier Transform Operator
γ	Deflection angle of biprism
h	Plank's constant
$\hbar$	$h/2\pi$
I	Irradiance (for light) current for electrons
K	Constant
k	wavenumber, $1/\lambda$
$\hat{k}$	Direction unit vectors
L	Distance traveled through field
κ	Spectrum coordinate relative to the nominar wave number k_0
λ	wavelength
λ_{inel}	Mean free electron path for inelastic collisions
m	Mass
m_o	Rest mass of electron
μ^{sc}	Spatial coherence function
μ^{tc}	Temporal coherence factor
n	Order of interference
Ω	Solid angle into which the electron source emits
P	Observation Point/Plane
P_{inel}	Probability of inelastic collision
p	momentum
Φ , φ	Phase of the wave/wave-packet
q_c	Fringe period
r	direction of wave propogation
ρ	Source size, source radius
S	Integration path
$s(k)$	Spectrum of the wave numbers
SNL	Sandia National Laboratories

t	Time
U	Accelerating potential, electric potential
$V_{Biprism}$	Biprism voltage
v	Fringe velocity
v	Particle velocity
ν	Doppler frequency
$\mathcal{V}$	Fringe visibility
x_s,y_s	Source location
x_d,y_d	Coordinates in the detector plane

[PAGE PURPOSELY LEFT BLANK]

1. INTRODUCTION

Making dynamic measurements at the nano-scale will become increasingly important as areas of research as disparate as materials research to nano-machines are pursued. This is demonstrated by the valuable information gained by dynamic studies of Microelectromechanical systems (MEMS). The same sort of insight, design information, and physical interactions are even less well understood in the nano-realm. It is thought that by designing a truly dynamic nano-scale device, broad new areas of research could be opened up in nano-dynamics.

Building on the vast amount of work done to develop transmission electron microscopes (TEM), a Doppler electron velocimeter (DEV) is envisioned to open up this important field of nano-dynamics. This is assisted by the fact that analogs of nearly all of the traditional optical equipment are available including: coherent sources, beam-splitters, bi-prisms, lenses, imaging systems and detectors. These have been developed and optimized for situations other than for the DEV, so further development and modification of these will be required.

The theoretical background for the DEV has already been established [1, 2], and this SAND report reviews the work done in FY2008 to attempt to determine whether it is technically feasible. The key aspect to this is answering the question: what are the measurement bandwidth limitations of the DEV? The answer to this question revolves around the joint issues of electron beam coherence and maximum available source current. These two questions are considered in light of realistic and existing electron microscope equipment including electron sources and detectors. Section 1 gives a brief overview of electron waves and electron holography. Section 2 develops the theory and mathematical equations behind the implementation of a Doppler electron system. Work done on an optical analog system showing that Doppler signals can be increased with single point measurements is covered in Section 3. The development and testing of a high-bandwidth and low beam-current dynamic electron detector is in Section 4. Finally, Section 5 briefly outlines types of experiments and ranges of dynamic behaviors that could be measured by a 1-MHz Doppler electron system.

1.1. Doppler electron background

An extremely short review of the concepts required to understand electron holography will be outlined in this section. This includes a discussion of the wave-particle duality, the meaning of particle waves, and the understanding of interference of electrons. For more depth please see Reference [1].

1.1.1. de Broglie waves

In 1924, Louis de Broglie postulated that if light was a particle (a photon), then maybe electrons can be viewed as waves. Indeed, any particle (defined as a thing with mass) has a wave description, although for large (heavy) objects, the wavelength is infinitesimally small and not observable. Large is a bit of a euphemism; large for these purposes is really anything larger than an electron, proton, neutron, or atom. The famous de Broglie equation relating momentum and wavelength is:

$$p = \frac{h}{\lambda}, \tag{1.1}$$

where p is the momentum, h is Plank's constant and λ is the wavelength. Combining this with the relativistic expression for momentum, the wavelength of an electron can be calculated as:

$$\lambda = \frac{hc}{\sqrt{E^2 - m_o^2 c^4}}, \qquad (1.2)$$

where c is the speed of light, m_o is the electron rest-mass, and E is the electron energy. In an electron microscope the energy is supplied by an accelerating potential in the microscope column. Simplifying Equation (1.2) and including the microscope accelerating voltage U, an equation relating the electron wavelength and the accelerating potential can be found:

$$\lambda = \frac{1.226}{\sqrt{U(1 + 0.9788 \times 10^{-6} U)}} \text{ (nm)}. \qquad (1.3)$$

This states that, the wavelength can be directly controlled by the accelerating potential. Table 1 contains some typical accelerating potentials and their resulting wavelengths. As can be seen, wavelengths in the picometers are rather easily obtained. The extremely short wavelengths have the advantage of avoiding the diffraction limitations inherent in laser based velocimeters. This, and the availability of sources and optical components for electron waves, makes the electron microscope attractive as a potential velocimeter test bed.

Table 1. Sample electron wavelengths and electron microscope accelerating potential.

Acc. Potential U (kV)	Wavelength λ (nm)	Wavenumber *k* (1/nm)	v/c
0.1	0.12264	8.154	0.01978
100	0.00370	270.163	0.54822
500	0.00142	703.594	0.86286
1000	0.00087	1146.886	0.94108
2000	0.00050	1982.858	0.97907

1.1.2. Interference of electrons

As outlined, the de Broglie wave can describe the motion of everyday particles as waves, or maybe more accurately, wave packets. In everyday physics, this applies to light by means of the photon concept, which being both a boson and massless has some properties that heavier particles do not exhibit. The interference of electrons is not nearly as straightforward as for photons, because the wavelength is a variable dependent on a number of factors, including the electric and magnetic fields it travels through in the microscope, via the Lorentz force. This dependence leads to the strange idea that the wavelength and frequency of the electron are not clearly defined. Fortunately, this is not important as neither of these quantities are directly measurable. Furthermore, diffraction patterns *are* clearly seen in TEM work—and leads directly to the conclusion that electron waves can interfere even if their wavelengths are not clearly defined. The fundamental physics behind this is that interference is the measurement of the change of phase ($\Delta\phi$) as two waves travel through space and are recombined; or it is, alternately thought of as the interference of two virtual point sources at the detector as illustrated in Figure 1. The source A is split into to virtual sources, A_1 and A_2 by means of a biprism or beam splitter. This is the fundamental concept of all interferometric arrangements, whether optical or particle, such as the well known Michelson and Mach-Zehnder interferometers. Using the idea of two virtual sources, the interference of electrons can be described mathematically with the following reasoning.

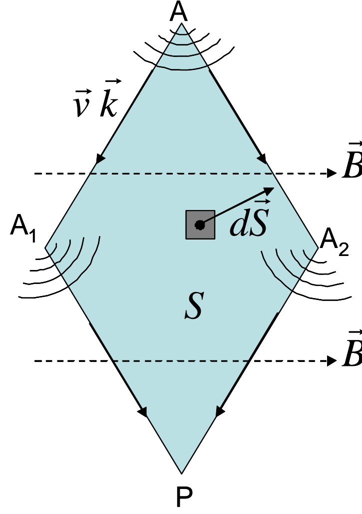

Figure 1. Point source interference model.

Electrostatic and magnetic fields are typically thought of as acting on the momentum of particles, but this interaction can be generalized in wave behavior to a phase-shift. This phase shift can be found by integrating around the path AA_2PA_1A, as shown in Figure 1,

$$\phi_2 - \phi_1 = \int_A^{A_2} \hat{k} \times d\hat{r} + \int_{A_2}^{P} \hat{k} \times d\hat{r} - \int_A^{A_1} \hat{k} \times d\hat{r} - \int_{A_1}^{P} \hat{k} \times d\hat{r}\ , \tag{1.4}$$

where $k = 2\pi/\lambda$ often called the wave-number, and r is the direction of propagation. Using the canonical expression for momentum, which includes Maxwell's magnetic field term, where m is the mass, v is the velocity, e is the electron charge, and B is the magnetic field:

$$\hat{p}' = mv - e(\nabla \times \vec{B}) = \hbar\hat{k}\ , \tag{1.5}$$

and substituting Equation (1.5) into Equation (1.4), and simplifying via the Stokes theorem, an equation expressing the phase change of the electron wave as it passes through the sample can be found. Alternately, these equations can be derived from the Schrödinger equations, and using the WKB (Wetzel, Kramers, Brillouin) approximation for weak fields, the following phase shift equation can be formulated:

$$\phi_2 - \phi_1 = \frac{1}{\hbar} \oint \left(mv - e(\nabla \times \vec{B}) \right) \cdot d\hat{r}\ . \tag{1.6}$$

The line integral is carried out along the closed path of the interfering electrons (i.e., along AA_2PA_1A). Separating out the magnetic and electrostatic effects—the equation can be more easily understood as

$$\phi_2 - \phi_1 = \frac{1}{\hbar} \oint mv \cdot d\vec{r} - \frac{e}{\hbar} \int_S (\nabla \times \vec{B}) \cdot d\vec{R} = \frac{2\pi}{h} \oint mv \cdot d\vec{r} - \frac{e}{\hbar} \phi_m\ . \tag{1.7}$$

Inspecting Equation (1.7) in light of Equation (1.6), we can see that the relation $\vec{k} = p/\hbar = mv/\hbar$ remains valid even with the wavelength ambiguity discussed previously. This is true even in the presence of a magnetic field, which simply adds an offset ϕ_m to the phase change.

1.1.3. Möllenstadt electron biprism

That holography works with electrons is not under dispute and has been demonstrated for many years. Because of coherence issues, the Möllenstadt electron biprism (Figure 2) is the standard

interference arrangement for the TEM and is briefly explained here as an example of the interference of particle beams. The biprism is so termed because of its relation to the Fresnel optical biprism interference experiments. The biprism is one of a number of simple *wavefront* splitting interferometers that in essence creates two point sources in space from a single source. This arrangement helps ensure the temporal and spatial coherence of the overlapping beams and hence their interference by creating two virtual sources from a single source. One side of the beam may be passed through a sample, which then causes some phase shift in the wavefront, and then it is recombined with the reference wave to create an interference pattern. Information about the sample is obtained by measuring the phase change, $\Delta\phi$, as related in Equation (1.7). The interference effect is subject to a number of constraints, including the inherent coherence of the electron beam, both spatial and temporal. This concept is more thoroughly discussed in Section 2.

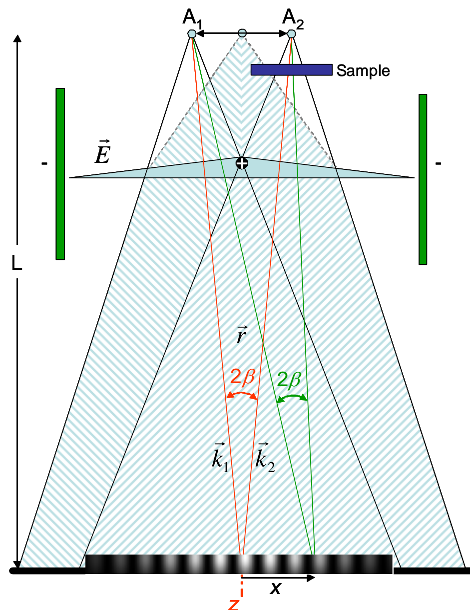

Figure 2. Möllenstadt biprism.

1.2 Applications for DEV

Equation (1.7) has a number of interesting implications. It says that the phase of an electron wave is sensitive to three different parameters; velocity, electric fields and magnetic fields. This can be a positive point, in that any of these three parameters can be measured by the DEV. A detailed survey of possible applications is discussed in Section 5. However, these phase effects are likely to cause problems when assembling an actual device. This is due to the extreme sensitivity of the electron interferometer and the effects of time-varying electric fields, magnetic fields, and the mechanical stability of the system.

2. THEORY

This section is reformatted from a report from Tom Milster, University of Arizona, for work done under contract to Sandia. Portions of the work have been reworked to better fit the flow of this report.

The following sections review the considerations required to form an electron velocimetry signal. Analysis described in Litche's recent review paper [3] is used as a model for the development. Section 2.1 reviews the analysis of a basic electron holography setup as applied to the DEV shown in Figure 3. Section 2.2 covers the basics of coherence as they apply to electron beams. This information is then mathematically presented in Section 2.3 – 2.4 and interpreted for the DEV. Finally, considerations for high-speed electron velocimetry are listed.

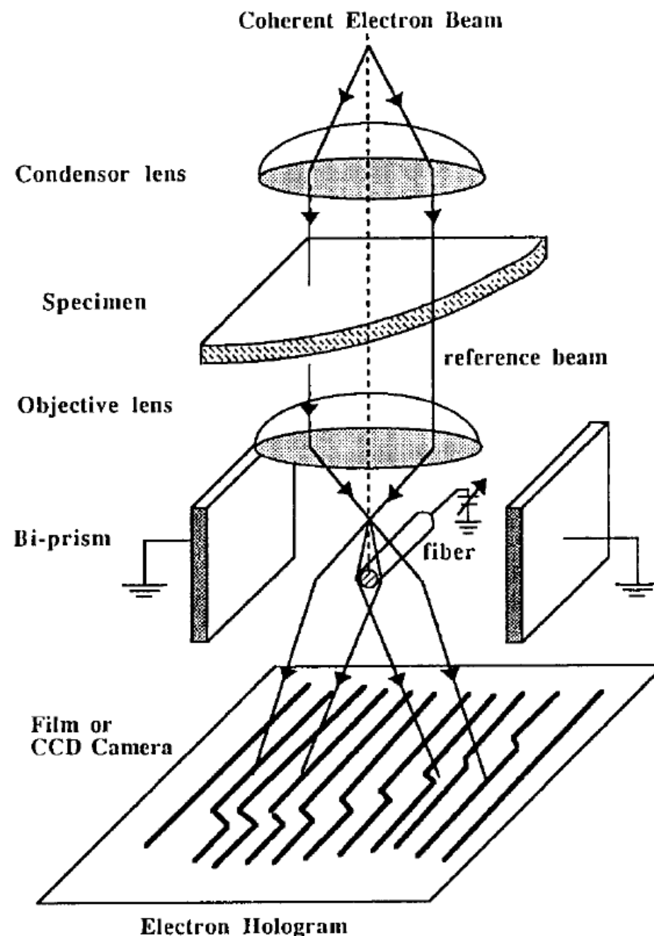

Figure 3. Schematic of biprism holography setup [4].

2.1. Analysis of Basic Electron Holography

A simplified ray diagram of basic electron holography without the object is shown in Figure 4. In this case, the electron gun is considered as a point source (A) generating a spherical wavefront. The biprism creates a linear phase shift outward from the center wire to the side of the chamber.

Two virtual sources A_1 and A_2 are created from the source A's spherical wavefront passing on each side of the biprism. The deflection angle γ due to the linear phase shift is constant for each ray emitted from the source. Two rays, indicated by direction unit vectors $\hat{k}_1$ and $\hat{k}_2$, are deflected by the biprism toward the observation plane and meet there at the symmetry axis. The deflected direction unit vectors $\hat{k}_1'$ and $\hat{k}_2'$ appear to come from the virtual sources A_1 and A_2, respectively.

Since the angular deviation is very small, on the order of 10^{-4} radians, the relationships between α, β and γ are given by:

$$\beta = \frac{a}{b}\alpha , \tag{2.1}$$

$$\beta = \frac{2a}{a+b}\gamma . \tag{2.2}$$

By the time the spherical waves reach the observation plane (a + b = several 100 mm from the sources), the wavefronts are essentially planar over the small region of observation near the central axis, and the fringe period, q_c, is

$$\frac{1}{q_c} \approx \frac{1}{k_0\beta} , \tag{2.3}$$

where $k_0 = 1/\lambda$. In addition, the deflection angle γ is linearly proportional to the biprism voltage $V_{Biprism}$, such that $\gamma = \gamma_0 V_{Biprism}$. The biprism voltage is typically a few volts.

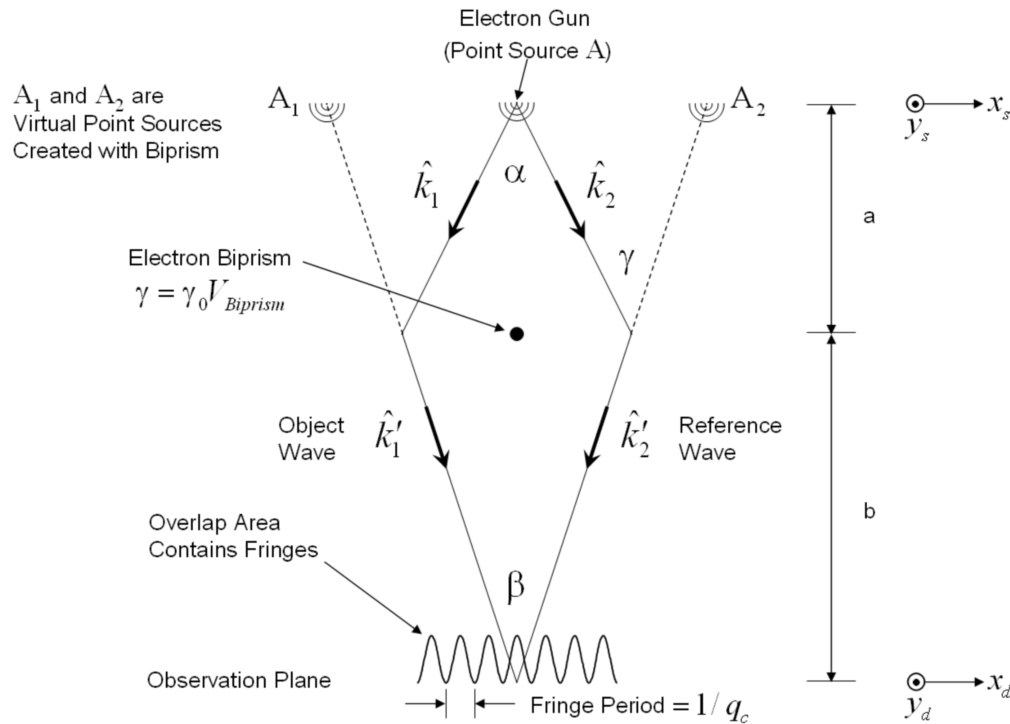

Figure 4. Simplified ray diagram of basic electron holography. The specimen is not shown.

Usually, the assumption is made that electron waves emitted from different areas of the filament or tip are uncorrelated with each other. If the emitted electrons have nearly the same energy, as shown in Table 2 for ΔE/E small, the emission of the tip is considered a *quasimonochromatic extended source*. That is, the time average combination of electron waves emitted from different parts of the filament do not produce any beat frequencies within the bandwidth of the detector. However, electron waves emitted from individual source points can pass through components, like beam splitters and prisms, so that parts of the same wavefront interfere and produce electron "fringes". The fringes are distributions of electron density. When several source points produce fringes in the detector plane, relative fringe shift can blur the aggregate fringe pattern. Like with an optical system, consideration of the source size, distance and energy (wavelength) distribution is called the *coherence* of the system, and it affects the *contrast* of the fringe pattern. Contrast is specified in terms of fringe visibility $\mathcal{V}$, as defined by

$$\mathcal{V} = \frac{I_{\max} - I_{\min}}{I_{\max} + I_{\min}}, \tag{2.4}$$

where $I_{\max}$ and $I_{\min}$ are maximum and minimum irradiance values in the fringe image, respectively. Coherence is reviewed more completely in Section 3. For the remainder of this section, electron beams are assumed coherent.

Table 2. Typical electron source brightness and beam currents.

Electron Beam Sources	Required Vacuum (Torr)	Virtual Source Diameter (μm)	Energy Width, ∇E (eV)	Acceleration Voltage (kV)	Measured Brightness, B (A cm^{-2} sr^{-1})	Current Density at Specimen (A cm^{-2})
Heated Field Emission	10^{-8}-10^{-9}	0.1	0.8	100	10^{7}-10^{8}	20
RT Field Emission	10^{-10}	0.002	0.28	100	2×10^{9}	4000
Hair-Pin Cathode	10^{-5}	30	0.8	100	5×10^{5}	1
Tungsten (W) Cathode	10^{-6}	10 – 50	1-2	100	1 to 5×10^{5}	3
LaB_6 Cathode	10^{-6}	5 – 10	1	75	7×10^{6}	14

2.2. Introduction to Coherence

By definition, a coherent source is one which exhibits interference when two parts of the wave are overlapped via an interferometer. One must take care of how this interference is discussed as there is some basic confusion due to the counterintuitive nature of many quantum mechanical effects. For instance, in optics, the wave is typically described as being split at the beam-splitter and then recombined at some imaging device to create interference fringes. For electro-magnetic radiation such as light, this is likely an apt description because the photon of light is a boson. Bosons have the property of being able to be densely packed and are able to theoretically interfere with each other. This aids the experimentalist in allowing an extremely bright coherent source, the laser for instance, where at any given location in the beam-path, there are likely photons which can interfere. Electrons, which are fermions, impose two important limitations on interferometry. First, electrons can only interfere with themselves. This means that to describe the interference the mathematics of the wave function must be used. The wave function, which represents the electron, is split by the beam-splitter and then recombined at a detector. What the

detector "sees" is the magnitude of the wave function, or the probability that the electron will be at any given location at some point in time. This has the consequence that electron holograms are built up by individual events accumulated over time to create the desired fringe pattern. This was most elegantly shown by Tonomura using an electron microscope [5, 6], and described by Feynman [7]. The same effect of course can be observed with photons, but the possibility of having a large number of photons at any given location (i.e., high flux or irradiance) results in having "instantaneous" fringes. This density of photons, as defined in per cell of phase space in quantum mechanical terms is called the degeneracy. Even for photons with degeneracies of the order of 10^{12} [7], there is a practical limit on the rapidity of the fringe formation due to the power of the laser, but for most optical applications, this is typically not the limiting factor. For electrons, the degeneracy is limited to 1, in other words, two electrons of opposite spin per unit-cell of phase space [8, 9]. This fundamentally limits the number of electrons per second from the source, or the brightness, B_{max}, to [10]:

$$B_{\max} = \frac{2e\Delta E}{h\lambda^2} \ (\mathrm{A{\cdot}cm^{-2}{\cdot}sr^{-1}}), \tag{2.5}$$

where e is the electron charge, ΔE is the source energy spread, h is Plank's constant, and λ is the electron wavelength. For a 300 keV electron and a degeneracy of 1, this leads to a maximum theoretical brightness of 3.9×10^{14} $\mathrm{A{\cdot}cm^{-2}{\cdot}sr^{-1}}$. Real sources have of course a lower brightness, typically in the range of 6×10^{9} $\mathrm{A{\cdot}cm^{-2}{\cdot}sr^{-1}}$.

This quantum mechanical assumption of fermion behavior is reinforced with the practical consideration that only one electron is traversing the interferometer at any given time. An electron spacing of 25 µm can be calculated by taking an electron beam with a current of 1 µA (a high current) and a velocity of 1.6×10^{8} m/s (100 kV). This gives an electron spacing, much longer than the coherence length of 7-µm, further confirming the single electron interference assumption. Once single electron interference is understood, it is easier to make some headway on understanding the concept of coherence in an electron interferometer.

Thinking about and explaining coherence and coherence limitations is often simplest in terms of Young's double slit experiment [11]. There are two inter-related types of coherence often termed transverse and longitudinal coherence. Both are illustrated in Figure 5 in relation to Young's double slit experiment. Transverse (or spatial coherence) is inversely related to the source size. That is, the smaller the source the greater is the transverse coherence. For interference to occur, the transverse coherence must be large enough to cover both holes of Young's interferometer. This is alternately described for larger non-ideal sources by taking the ideal point source and shifting it $\pm\rho$, to represent the true source size. This is the same as saying the real source is a combination of ideal sources emitting independently of one another. Translating the ideal source has the physical effect of shifting the resulting fringes $\pm\Delta x_d$ as illustrated in the figure. If the translation of the fields is such that the shift is one fringe, the resulting fringe summation will average out the fringes and the source is said to be spatially incoherent. The longitudinal coherence is related to the source energy spread, i.e. how monochromatic is the source. The more monochromatic the source (smaller energy spread) the longer the temporal coherence. Each wavelength represented in Figure 5 by λ_1, $\lambda_2 \ldots \lambda_n$, creates a set of fringes of differing widths. The contributions of each of the wavelengths are again summed to yield a final fringe contrast. As

can be imagined, if too broad a number of wavelengths contribute to the fringe formation, the contrast will decrease to zero. This physical description which imagines a single perfect source that can be varied in either wavelength or position is analogous to the more involved description of partial coherence introduced by Born and Wolf [12] and covered in Sections 2.3 and 2.4. However for the DEV, electrons emitted with identical energy, and from the same location on the source, each represents an ideal source. The separate fringes created by these ideal electron sources are coherent and can be summed up to create the final fringe contrast.

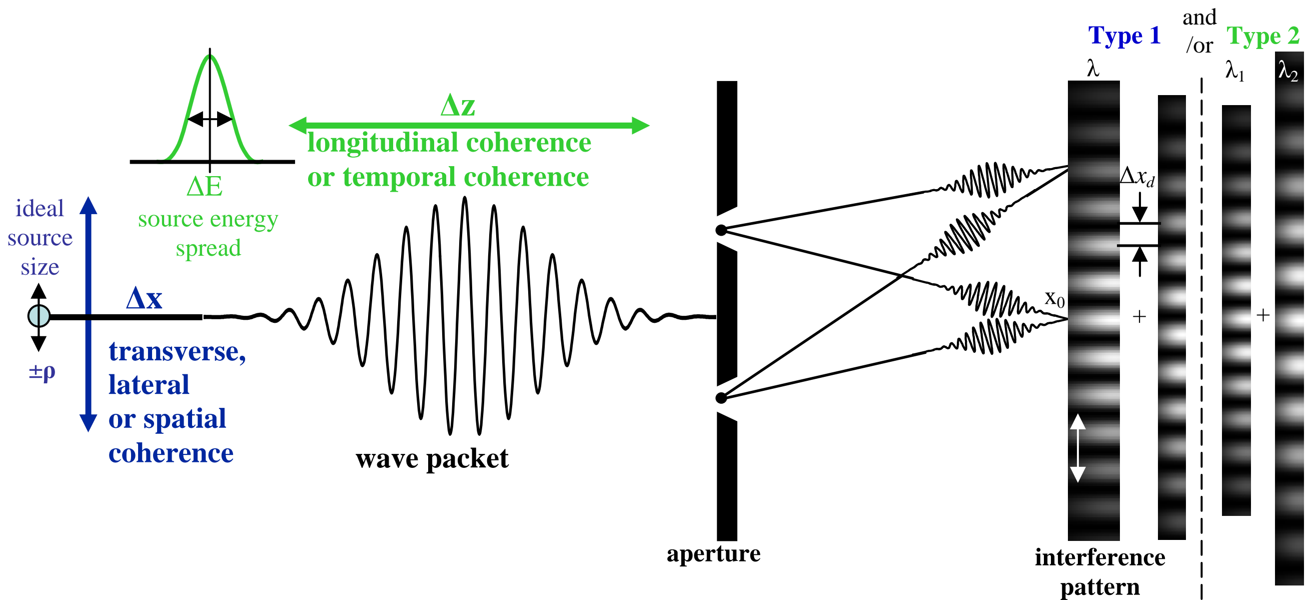

Figure 5. Young's double hole interferometer showing coherence effects on fringe contrast.

How does coherence affect the DEV? Longitudinal coherence is typically not a practical problem as sources with extremely small energy spreads are available (with some cost in beam current). Transverse coherence is generally considered more of an issue, not in that extremely small sources are not available, but the greater the transverse coherence required, the lower the resulting beam current. This current limitation directly influences the maximum fringe detection rate and therefore the bandwidth of the DEV. It is because of this current limitation that methods of circumventing the spatial coherence issues are being investigated.

2.3. Spatial Coherence

Initial discussion of fringe formation does not include the object, *i.e.* the object specimen is removed from the system. Fundamental limits of detection are derived based on fringe visibility due to source size and geometrical factors.

First, theoretical relationships for the fringe pattern are obtained for a centered point source at (x_s, y_s) = (0,0) with ΔE ~ 0. In this case, illustrated in Figure 4, the fringe pattern is nearly a

perfect cosine wave. Individual electron wavefronts from the object and reference waves are given by

$$U_1'(x_d, y_d) = \exp[-j2\pi k_0 \beta x_d / 2] \ , \tag{2.6}$$

and

$$U_2'(x_d, y_d) = \exp[j2\pi k_0 \beta x_d / 2] \ , \tag{2.7}$$

respectively, where (x_d, y_d) are coordinates in the detector plane with the biprism oriented in the x_d axis. Electron density is given by

$$I(x_d, y_d) \propto \left| U_1'(x_d, y_d) + U_2'(x_d, y_d) \right|^2 = 1 + \cos(2\pi k_0 \beta x_d) . \tag{2.8}$$

Next, a second source point B is added in the source plane at position $(x_s, 0)$, as shown in Figure 6. Since angles α, β and γ are unchanged, the fringe pattern due to source B exhibits the same period $1/k_0\beta$ as the fringes from source A. However, this second fringe pattern is shifted by an amount $\Delta x_d = x_s$. The net electron density at the detector plane is simply the sum of individual fringe patterns, because the time average of the wave combination from the two point sources results in no beat terms within the bandwidth of the detector. If the two source points exhibit the same brightness, this electron density is simply

$$I(x_d, y_d) \propto 2 + \cos(2\pi k_0 \beta x_d) + \cos[2\pi k_0 \beta (x_d - x_s)] \ . \tag{2.9}$$

Depending on the position x_s of source B, the net electron density exhibits varying visibility $\mathcal{V}$, as shown in Figure 7. When the maximum of the unshifted fringe aligns with the minimum of the shifted fringe, the electron density is uniform across the detector plane and $\mathcal{V} = 0$. When maxima of the individual fringe patterns align, $\mathcal{V} = 1$. Notice that the fringe period is not a function of the shift. The aggregate electron density *I,* exhibits the same period as individual fringes, although it may be scaled in amplitude with a dc offset.

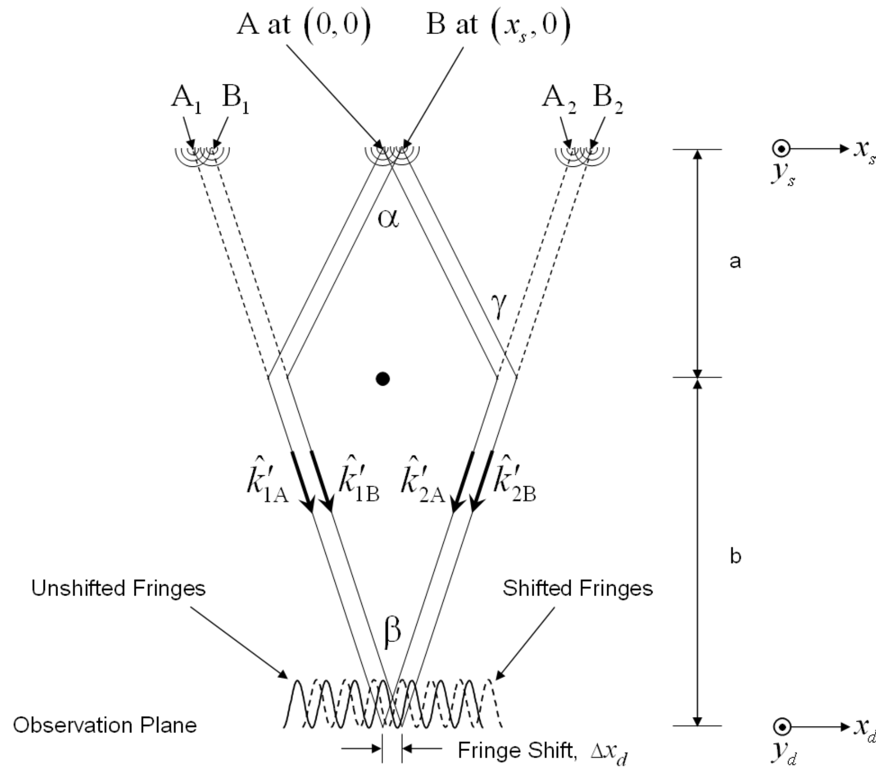

Figure 6. A second point source of electron waves (B) is added at location (x_s,0). The net result is a fringe shift Δx_d for the B fringes, where $\Delta x_d = x_s$. The resulting current density is the sum of individual fringe patterns

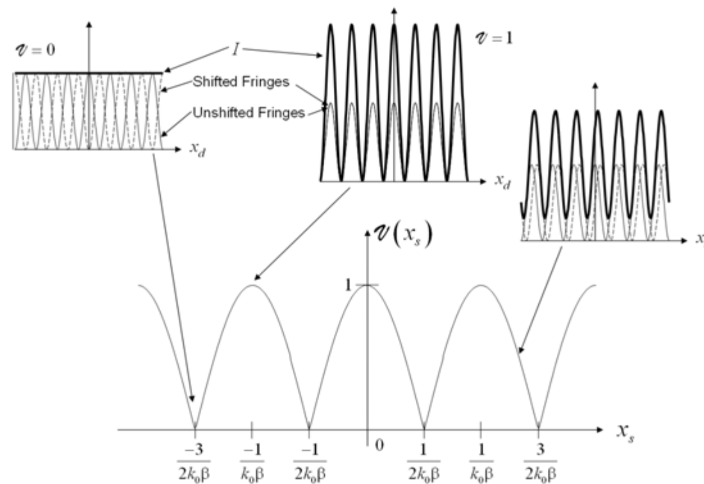

Figure 7. Visibility $\mathcal{V}$ as a function of x_s for the geometry of Figure 6.

If the source is extended with normalized distribution function $i(x_s, y_s)$, each point in the distribution produces a fringe in the detector plane. The aggregate detector pattern is the integration of individual fringes, where

$$
\begin{aligned}
I(x_d, y_d) &= K\iint_\infty i(x_s, y_s)\left[1+\cos\left(2\pi k_0\beta x_d + 2\pi k_0\beta x_s\right)\right]dx_s dy_s \\
&= K\left[1+\iint_\infty \cos\left(2\pi k_0\beta x_d + 2\pi k_0\beta x_s\right)dx_s dy_s\right] \\
&= K\left(1+\mathrm{Re}\left\{\iint_\infty i(x_s, y_s)\exp\left[j(2\pi k_0\beta x_d + 2\pi k_0\beta x_s)\right]dx_s dy_s\right\}\right) \\
&= K\left[1+\left|\mu^{sc}\right|\cos\left(2\pi k_0\beta x_d + \theta^{sc}\right)\right] \quad ,
\end{aligned} \tag{2.10}
$$

where

$$
\mu^{sc}(k_0\beta) = \left|\mu^{sc}(k_0\beta)\right| e^{j\theta(k_0\beta)} = \mathbf{F}^{-1}_{k_0\beta}\left[\int_\infty i(x_s, y_s)\,dy_s\right] , \tag{2.11}
$$

and $\mathbf{F}^{-1}$ represents the inverse Fourier transform of the argument and $k_0\beta$ is the transform variable. The constant K in Equation (2.10) is unimportant for relative comparisons. Equation (2.11) defines the *spatial coherence function* μ^{sc}, whose magnitude reduces aggregate fringe visibility and whose phase shifts the aggregate fringe pattern. In fact, since the waves in the reference and object paths are assumed equal in electron flux, $\mathcal{V} = \left|\mu^{sc}\right|$.

The development of Equations (2.10) and (2.11) is made without an object specimen. Therefore, these equations represent the best possible result of experimental visibility. If $\mathcal{V}$ is too low (say < 0.2), it will be difficult to measure any type of fringe pattern with an object specimen present.

Equation (2.11) can also be written as a function of the angular subtense-α at the source of the two respective waves. From Equation (2.3),[1]

$$
\mu^{sc}\left(\frac{\mathrm{a}}{\mathrm{b}}k_0\alpha\right) = \left|\mu^{sc}\left(\frac{\mathrm{a}}{\mathrm{b}}k_0\alpha\right)\right| e^{j\theta^{sc}\left(\frac{\mathrm{a}}{\mathrm{b}}k_0\alpha\right)} = \mathbf{F}^{-1}_{\frac{\mathrm{a}}{\mathrm{b}}k_0\alpha}\left[\int_\infty i(x_s, y_s)\,dy_s\right] . \tag{2.12}
$$

Given an electron source and microscope geometry, it is instructive to determine the amount of coherent current available at a given degree of spatial coherence. The electron source is characterized by its brightness B, which is the current emitted per unit area A and solid angle Ω,

$$
B = \frac{I}{A\Omega} . \tag{2.13}
$$

If the source distribution $i(x_s, y_s)$ is Gaussian with

[1] The relationship in Equation (2.3) is slightly different than that derived by Litche [3], in that it contains the factor a/b, which is not in the Litche development.

$$i\left(x_s, y_s\right) = \frac{1}{\sqrt{\pi}\rho_g} \exp\left[-\left(\rho/\rho_g\right)^2\right], \qquad (2.14)$$

the effective area of the source is

$$A = \pi\rho_g^2 \qquad (2.15)$$

The solid angle Ω is approximately the solid angle associated with the interacting wavefronts, where

$$\Omega \approx \pi\alpha^2 \qquad (2.16)$$

Application of Equation (2.12) yields

$$\mu^{sc}\left(\frac{\mathrm{a}}{\mathrm{b}} k_0 \alpha\right) = \exp\left[-\left(\pi \frac{\mathrm{a}}{\mathrm{b}} k_0 \alpha \rho_g\right)^2\right]. \qquad (2.17)$$

Combination of Equations (2.13) and (2.15)-(2.17) yields

$$I^{sc}\left(\mu^{sc}\right) = \left(\frac{b}{a}\right)^2 \frac{B}{k_0^2} \ln\left(1/\left|\mu^{sc}\right|\right) \qquad (2.18)$$

for the total current available at a given degree of spatial coherence. Since the brightness increases linearly with acceleration voltage and $k_0 = 1/\lambda \sim \sqrt{V_a^*}$ from Equation (1.3), the ratio B/k_0^2 does not depend on acceleration voltage. The spatial coherence factor μ^{sc} depends on V_a^* in that lower k_0 increases μ^{sc} in Equation (2.17).

As an example, consider the RT Field Emission tip in Table 2 with B = 2x10^9 A/cm^2/sr, ρ_g = 1 nm, α = 0.8 mrad and V_a^* = 100 kV. If b/a = 1, μ^{sc} = 0.63 and I^{sc} ~ 0.1 nA.

Consider the presence of an object specimen that only shifts the phase of the object wave, without any decrease of transmitted electron energy or amplitude. If an appropriate grating is placed in the detection plane, such that it aligns with the fringes and passes electrons through to an integrating detector, variations in the transmitted phase result in variations in detector current. Under the best conditions of 100% efficiency and all I^{sc} electrons contributing to the maximum signal, about 0.1 nA (or N=6.24x10^8 electrons per second) are detected when the grating and fringes are perfectly aligned. DEV assumes a time-varying signal, which might be a periodic variation in transmitted phase through the object specimen. If the signal bandwidth is 1 MHz, then approximately 600 signal electrons are available during each cycle of the vibration. The Poisson-noise, or shot noise, can be calculated using:

$$\sigma = \sqrt{2eI^{SC}\Delta f}\ , \tag{2.19}$$

where σ is the Poisson noise in Amps, e is the electron charge, I^{sc} is the average current and ∇f is the bandwidth of interest. This is approximately the same as the simpler calculation [13]:

$$SNR = \sqrt{N} \tag{2.20}$$

Thus, considering only spatial coherence, a Poisson-noise-limited DEV system operating at 1 MHz under ideal conditions will experience a maximum signal-to-noise ratio of about 25.

2.4. Temporal Coherence

Section 2.3 assumes that wavelengths of individual source emitters are essentially equal. Of course, this condition can not be strictly true, because then all waves would necessarily be coherent. Instead, the emission area has a finite bandwidth of wavelengths associated with the energy spread ΔE of the emitted electrons, as shown in Table 2. Typically, ΔE ~ 1eV. A 1eV shift in the energy of the electron at 100-kV acceleration voltage produces a wavelength change of about 10^{-5} nm.

Although there is a spread in the wavelengths emitted from the source, each emitted electron wave has only one energy value and associated wavelength. Therefore, each electron wave is passed through *both* object and reference paths of the interferogram-generating electron optics and will produce a fringe pattern, but the fringe patterns from different electron waves will have slightly different period. Because the system is otherwise symmetric, the center points of all fringe patterns are aligned. The aggregate effect of adding fringe patterns with different periods is that, as distance increases away from the symmetry point, fringe contrast decreases as illustrated in Figure 5.

A development similar to that used for Equations (2.10) and (2.11) can be used to show that the energy spread ΔE produces an additional coherence factor μ^{tc}, which is called the *temporal coherence factor*. μ^{tc} is calculated by

$$\mu^{tc}(n) = \left|\mu^{tc}(n)\right| e^{j\theta^{tc}(n)} = \mathbf{F}_n^{-1}\left[\int_\infty s(\kappa)\exp\left(i2\pi\kappa n/k_0\right)d\kappa\right], \tag{2.21}$$

where n is the order of interference, $s(k)$ is the spectrum of wave numbers and $\kappa = k - k_0$ is the spectrum coordinate relative to the nominal wave number k_0, where $\kappa \ll k_0$.

If the energy spectrum is approximated with a simple rectangular function of width Δk, the temporal coherence function is

$$\mu^{tc}(n) = \frac{\sin\left(\pi\frac{2n\Delta k}{k_0}\right)}{\pi\frac{2n\Delta k}{k_0}} = \frac{\sin\left(\pi\frac{n\Delta E}{V_a^*}\right)}{\pi\frac{n\Delta E}{V_a^*}}, \tag{2.22}$$

since $\frac{\Delta k}{k_0} = \frac{\Delta E}{2V_a^*}$. For ΔE = 1 eV and V_a^* = 100kV, $n \sim 10^5$ before the first zero in visibility. For interference experiments and holography, which use $n \le 500$ at most, temporal coherence does not pose any problem.

When combined with contrast reduction due to spatial coherence, a reasonable approximation to the combined fringe pattern of Equation (2.10) without the object specimen is

$$I\left(x_d, y_d\right) = K\left[1 + \left|\mu^{sc}\right|\left|\mu^{tc}\right|\cos\left(2\pi k_0 \beta x_d + \theta^{sc} + \theta^{tc}\right)\right] . \tag{2.23}$$

However, for DEV, a restriction on the maximum amplitude of the phase disturbance is implied by temporal coherence. In the example above where maximum $n \sim 10^5$, *the maximum range of displacement for an object in reflection is about* $\lambda x10^5 \sim 0.18\ \mu m$. This estimate is made without regard to inelastic energy loss, as discussed in the next section.

2.5. Application of Theory to Inelastic Energy Loss

If the electron waves interact with static electric or magnetic fields, there is no energy loss. However, *inelastic* collisions with matter and dynamic fields cause a change in the electron wave energy. If the energy change is small, Equation (2.8) can be rewritten as

$$I\left(x_d, y_d\right) \propto 1 + \cos\left(2\pi k_0 \beta x_d - 2\pi \nu t\right) \tag{2.24}$$

where

$$\nu = \frac{\delta E}{h}, \tag{2.25}$$

where δE is the energy loss associated with the interaction. Note that the effect of inelastic collisions *in only the object specimen path* of the interferometer is completely different than the effect of temporal coherence, where energy differences at the electron source travel along both paths. With inelastic interactions in the object specimen, the net effect is that fringes move along a direction perpendicular to the fringe lines at a velocity

$$v = \frac{\nu}{k_0 \beta}. \tag{2.26}$$

Fringes can be detected if the integration time of the detector is short enough. Considering finite detector integration time, τ, an additional decrease in fringe visibility is given by

$$\left|\mu^{\delta E}\right| = \frac{\sin\left(\pi \nu \tau\right)}{\pi \nu \tau}, \tag{2.27}$$

which has its first zero at $\tau = 1/\nu$. Consider the case where ν = 1 Hz (δE = 4.135x10^{-15} eV). If $\left|\mu^{\delta E}\right|$ = 0.5, τ ~ 0.6 sec. Given the RT Field Emission tip example of Section 2.3, about 3.7x10^{8} electrons are available for detection. As mentioned in Litche [3], concerning this example,

> "… one would need such short exposure times that the number of collected electrons is very low, hence the signal disappears in quantum noise."

However, that application is for a distributed interferogram with an object specimen, where the entire interferogram must be recorded and processed in a computer in order to obtain information about the object. If a 1024 by 1024 pixel detector is used to collect the interferogram image, the average number of electrons per pixel in this example is approximately 350, which yields a Poisson signal-to-noise ratio of 18. For computer processing, this signal-to-noise ratio is acceptable, but a lower signal-to-noise ratio might be difficult to process.

For the DEV system, signal electrons can be integrated for a much higher signal-to-noise ratio and a higher detection bandwidth, as described in Section 2.3. If ν = 1 MHz, δE = 4.135x10^{-9} eV, and a signal-to-noise ratio of about 25 can be achieved under ideal conditions.

By comparison, inelastic interactions with matter are many orders of magnitude greater energy. For excitation of photons, δE is typically meV, plasmons at several eV and inner-shell excitations at several 10-eV. For these interactions, direct application of DEV is not practical. The frequency of the fringe motion associated with the inelastic energy loss is much higher than the detection bandwidth.

Not all electrons interacting with an object experience inelastic collisions. These collisions occur with probability P_{inel} given by

$$P_{inel} = 1 - \exp\left(-d / \lambda_{inel}\right), \tag{2.28}$$

where the object specimen thickness is d and the mean free path for inelastic collisions is λ_{inel}. Wave energy arriving at the detector plane then provides a uniform detected background to the electron density distribution, which lowers fringe contrast by a factor

$$C_{inel} = \exp\left(-d / 2\lambda_{inel}\right). \tag{2.29}$$

3. LINNIK MICROSCOPE EXPERIMENTS

One possibility for improving the beam current is to find a method of reducing the DEV spatial coherence requirements. This would allow a larger aperture to be used and therefore a greater current. This has been shown to work in the optical domain with an arrangement often referred to as a Linnik microscope [14]. This traditional Michelson arrangement uses an LED as a light source for measuring out-of-plane motion of an object. The setup and optical arrangement of a Linnik system is more difficult, due to the requirement of matching the path length between the object and reference legs as well as aligning the image from both legs. Figure 8 shows this pictorially with the microscope in imaging mode. The easiest way to visualize how this works is by thinking of the source as having areas of coherence, that if aligned will interfere. This is not unlike a speckle pattern in digital speckle pattern interferometry (DSPI). Using this setup with light, Doppler signals have been obtained. To increase the signal at the detector, the source was focused onto the object and reference and then aligned onto a single point detector with the result of increased Doppler signal, the so-called critical illumination case. This implies via analogy, that a less than perfectly coherent source can potentially be used for obtaining Doppler signals with an electron microscope. The importance of this conclusion is that loosening the coherence requirement will mean that greater current is available at the detector, which in turn increases the bandwidth of the detector.

3.1. Introduction to the Linnik microscope

The Linnik microscope is a well known interferometric arrangement that allows the use of a narrow band, yet spatially incoherent source to be used for interference experiments [14]. This arrangement, seen in Figure 8 is much like a Michelson interferometer and as such is ideally arranged to measure out-of-plane motions.

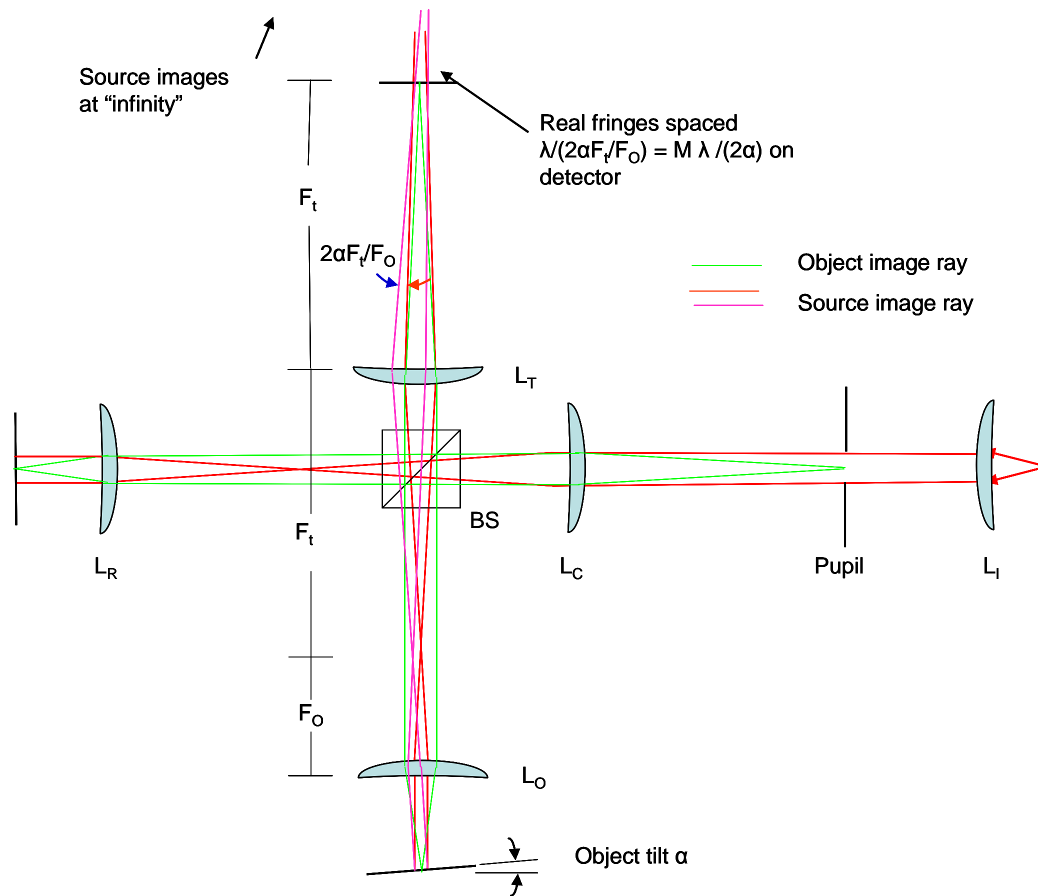

Figure 8. Point source ray diagram of Linnik Microscope

In the traditional setup, the microscope is arranged with a light source collimated by lens L_I. The illumination is then split by an amplitude splitting beam splitter with a reference and object leg with carefully matched path lengths. The matching of the path lengths is important because the source, a green LED in our experiment, has a short coherence length, typically on the order of tens of microns. This is fairly easily accomplished experimentally by exactly matching the optical paths and components in the two legs. In our experiments, this was done by having lenses L_O and L_R be identical Mitutoyo infinity corrected microscope objectives. As previously mentioned, the light is collimated by the first lens and then imaged at infinity on the object, a small moving mirror, and a reference mirror. The light is then recombined at the beam splitter and magnified onto a CCD camera via a simple tube lens. When the system is aligned and the path lengths are matched, high contrast fringes can be produced as shown in Figure 9. If the object moves out-of-plane, the fringes will move back and forth depending on the direction of motion. If a single point detector is put into the area of a bright fringe, a Doppler single can then be measured for this simple experiment.

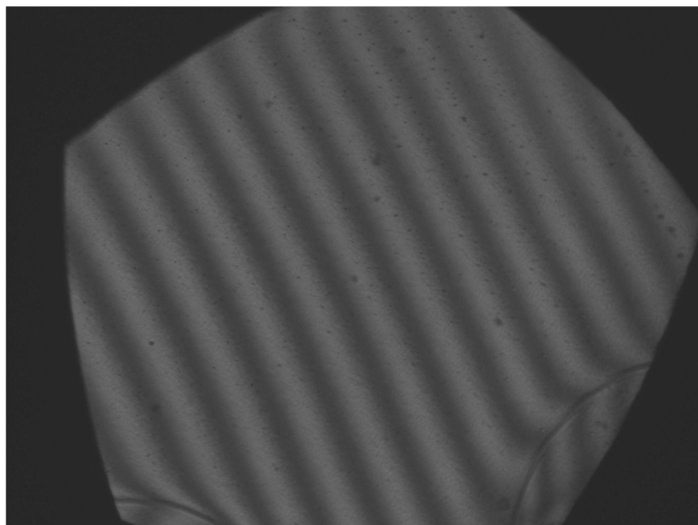

Figure 9. Collimated LED looking at a small mirror. A slight tilt is added to the object to create the fringes. Field-of-view is approximately 330 μm.

As previously mentioned, increasing beam current is one of the hurdles to detecting fast moving fringes. On this topic, note that much of the energy for the Michelson interferometer is wasted, because it is spread out over the entire viewing area. What would happen if all of the energy were focused on a single spot on the object, and then refocused on a single detector: would a higher signal be available at the detector?

3.2. Improving beam current via imaging the source

With this goal in mind, the Linnik microscope was modified from a collimated source to a source imaged into the pupil and then imaged onto the object and reference mirrors. The imaged source was then recombined at the detector. A schematic the critical illumination arrangement is shown in Figure 10. Three experiments were conducted with the results shown in Table 3. The first case used a bare LED in the illumination aperture and yielded a Doppler signal of 7 mV. The traditional collimated arrangement shows an improvement in Doppler signal to 31 mV. Finally the imaged LED, where all of the source energy is collected and imaged on the object and reference mirror gives a gain in the peak-to-peak Doppler signal level to 54-100 mV.

Table 3. Doppler signal level for different Linnik configurations.

Configuration	Mean mV	Doppler p-p mV
Bare LED	-4	7
LED collimated via single objective	-35	31
LED imaged via 2 lenses (Critical illumination)	-211	54 to 100

This particular optical analogy is related to electron holography via what is called Electron Beam Diffracted Interferometry (EBDI). This configuration including an amplitude splitting BS and a recombining biprism has been shown to be successful in the literature [15, 16]. The arrangement has been successfully demonstrated in a Hitachi HF-2000 electron microscope, which is a commercially available system especially optimized for electron holography. The typical arrangement has the electron beam impinging on a crystal after traversing the first objective

lens—the crystal acts as an amplitude splitting beamsplitter. The diffracted beams travel through the microscope to the biprism, where the voltage field is set to deflect the beams at the complementary and opposite angle to the crystal diffraction to overlap them. Herring [16] specifically mentions the possibility of using this arrangement with a spatially incoherent extended source, for the reasons already outlined in this paper.

3.3. Wavefront splitting versus amplitude splitting

To mimic the wave-front splitting function of the electron biprism, a wave-front splitting mirror was used, rather than the amplitude splitting mirror used in the previous experiments as illustrated in Figure 10. This was accomplished via a half-silvered cube shown in Figure 11. A laser rather than a diode was used in this arrangement to simplify any temporal coherence questions, and the laser spot was focused into the field stop. With this arrangement, almost no Doppler signal resulted. This is because the beam splitter acts as a spatial filter. The logic implied in the ray diagram in Figure 10 works on-axis only. If you consider a simple coherent imaging system with the pupil split in half, you get the essentials of the interferometer, with the Doppler phase existing as a difference between the top and bottom halves of the pupil. But the focal spot can be considered to be the sum of the diffraction patterns from the top and bottom halves. As diagrammed in Figure 12, this can be viewed as the wide focal spot from the half aperture, upon which is superimposed a set of fringes. When the half apertures are in phase, the fringes serve to narrow the focal spot. But when they are out of phase, the fringes split the focal spot as shown in the bottom diagram, and in Figure 13. For this reason, the current electron microscope arrangement with two beam splitters, i.e. wave-front splitting will not work. Fortunately this is not the only possible arrangement in an electron microscope. Using the amplitude splitting components in conjunction with a biprism, it may be possible to create a Mach-Zehnder interferometer that would work along the lines of the Linnik microscope. This would allow both a single point measurement and the use of an extended source.

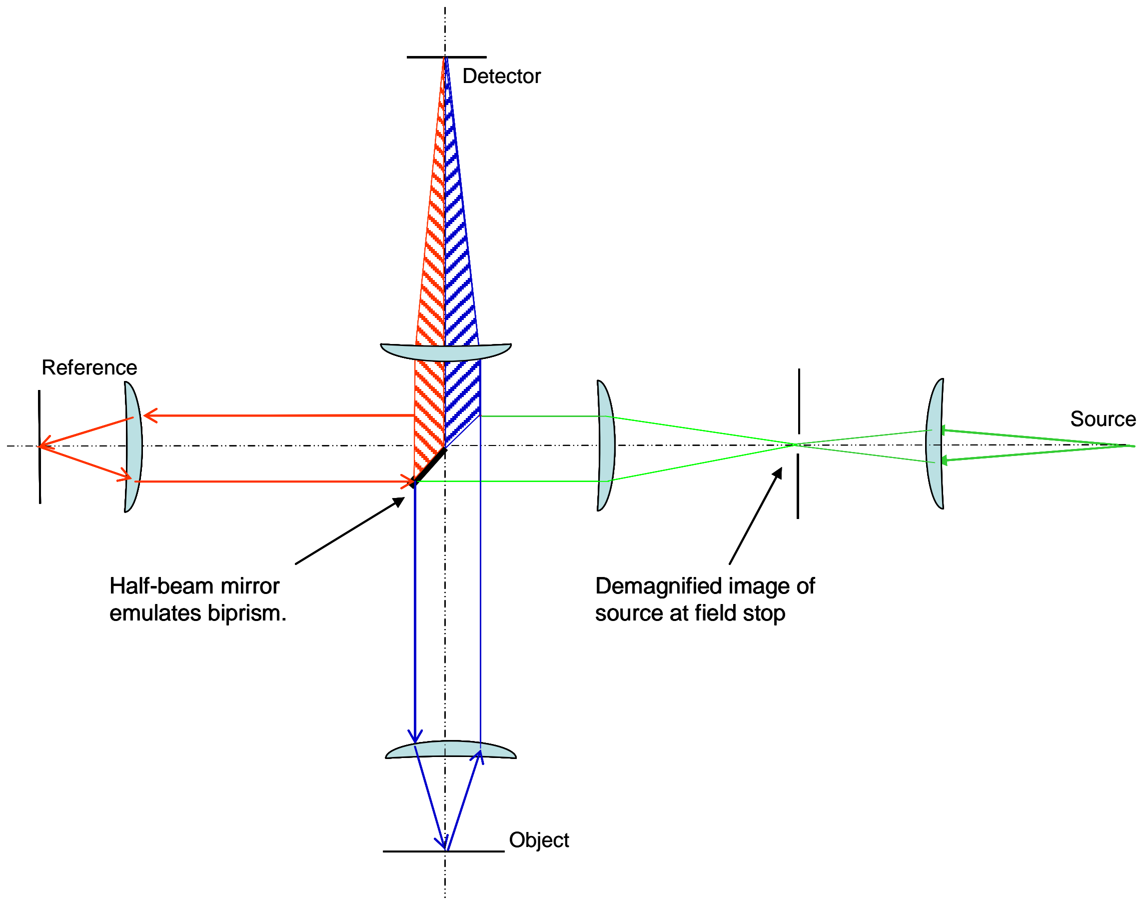

Figure 10. Linnik microscope set-up in a critical illumination case with the source imaged at the pupil and again on the reference and object legs. The wavefront splitting mirror is shown in the center.

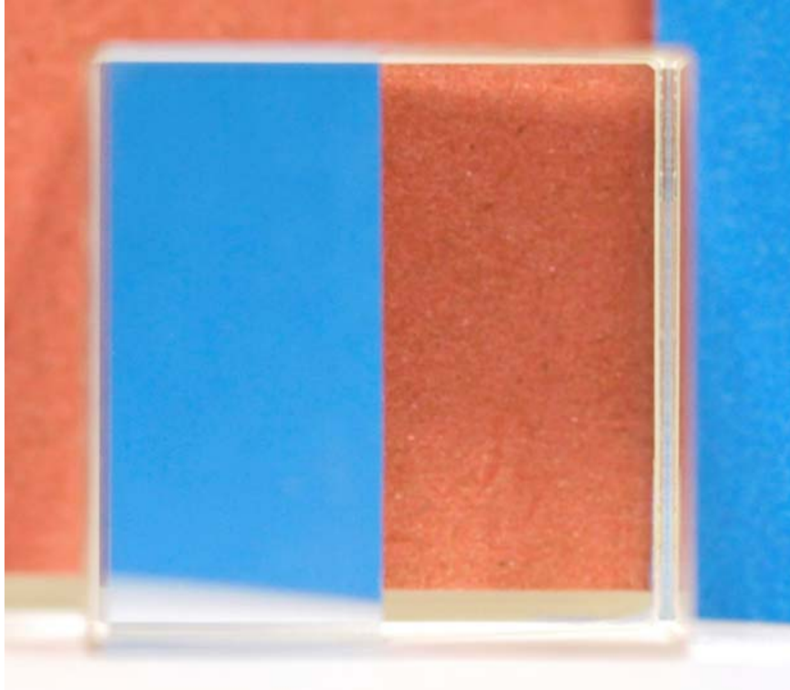

Figure 11. Photo of wave-front splitting half-silvered mirror.

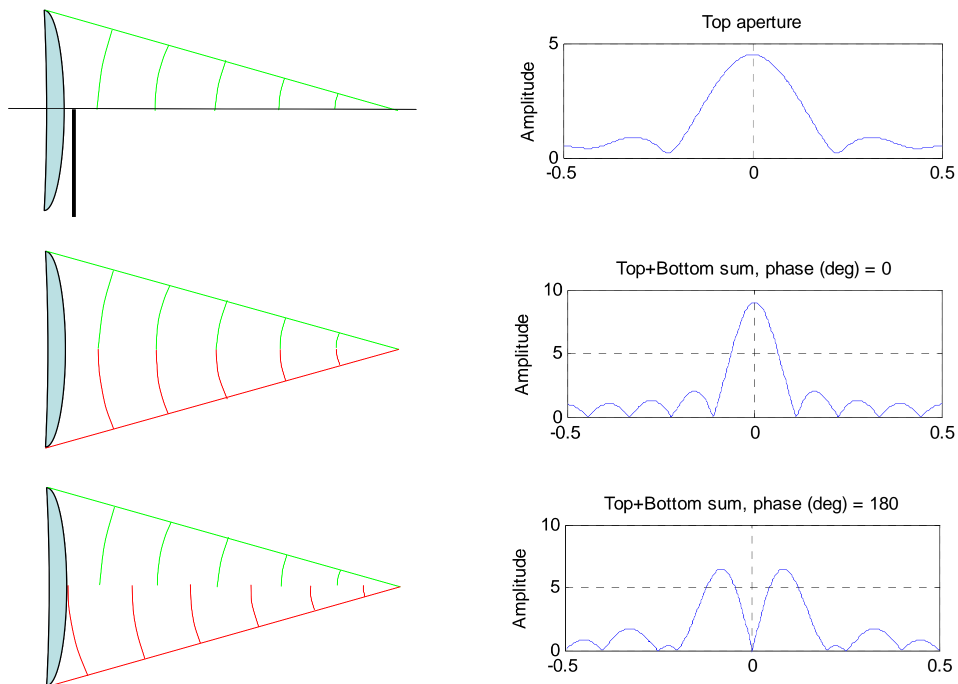

Figure 12. Diagram and resulting amplitudes at the detector for a wave-front splitting arrangement.

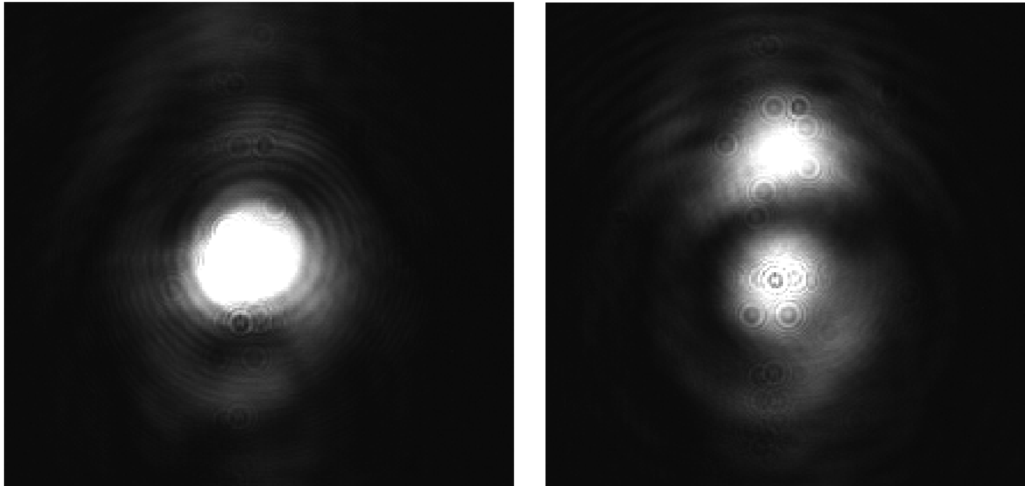

Figure 13. Focal spot of split-beam interferometer, with beams in and out of phase

3.4. Conclusions

The proposed EBSD arrangement for electron holography has some potential problems. The strength of the proposed optical arrangement is of course the increase of current at the detector, while not requiring a spatially coherent source. However, to maintain fringe contrast system stability will likely be important. Ongoing research is being conducted to analyze the optical analog and its application in electron microscopes to answer this question. Even with this arrangement beam current may still be too limited to detect the Doppler frequencies of interest.

Theoretical and mathematical derivations of the Linnik microscope as applied to a Doppler electron system are contained in Appendix A.

[Page purposely left blank]

4. ELECTRON DETECTION EXPERIMENTAL WORK

The successful outcome of this research is predicated on the development of a fast and low current electron detector. For TEM work, nearly all detectors are of the imaging type, either having a CCD camera looking at a phosphor screen, or a CCD with a micro-channel plate amplifier in front of it. For single point measurements, these are of course inappropriate. For single-point detection, which is more commonly used in SEM's, there are four main detector types: the Faraday cup, the Everhardt-Thornley detector, solid-state detectors, and electron multipliers.

The Faraday cup detector is simply a conductor which absorbs a certain number of electrons as the electron beam impacts it. The physical arrangement is such that the electrons pass through a hole that is small enough to ensure that the back-scattered electrons do not escape, therefore maximizing the captured current. The material is also chosen such that it has a low scattering coefficient leading to more primary electrons being absorbed.

The Everhardt-Thornley (ET) [17] is the most common detector used in an SEM and is shown in Figure 14. It can work in a number of different modes depending on the Faraday Cage bias. The bias can be set negatively to attract back-scattered electrons or positively to attract secondary-electrons. Once inside the Faraday cage, the electrons are accelerated onto the scintillator. The resulting photons travel down the waveguide and impinge on the photocathode. This releases an electron which then is amplified in the electron amplifier, resulting in a current output signal.

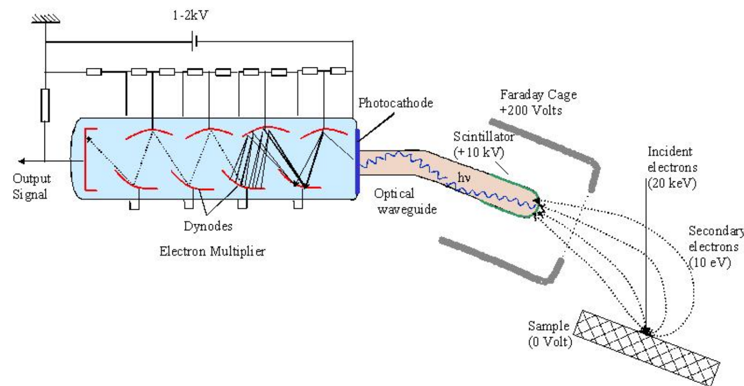

Figure 14. Schematic of an Everhardt-Thornley secondary electron detector (http://commons.wikimedia.org/wiki/Category:Secondary_electron_detector).

Solid state or semiconductor detectors work on the principle of the creation of an electron-hole created by the incident electrons. The energy of the incident electron can create a number of holes, which if not separated from the electron will recombine. The external bias applied to the thin surface metal supplies this and creates an amplified current at the output. One potential drawback to this is the relatively high capacitance of the detector limits its bandwidth [18].

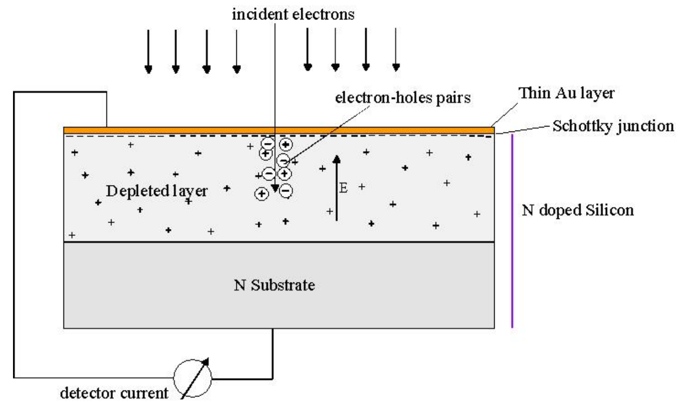

Figure 15. Schematic of a solid state detector.
(http://commons.wikimedia.org/wiki/Image:Solid_state_electron_detector.JPG)

Electron multipliers have been around and in different forms for many years. They are an integral portion of the Everhard-Thornley detector and micro-channel plates. They work by taking an incoming electron which strikes the internal surface of the multiplier and releases multiple secondary electrons. The voltage bias drives the electrons down the multiplier tube causing a cascading effect resulting in an amplified current at the output. A picture of an electron multiplier and the corresponding cascade schematic is shown in Figure 16.

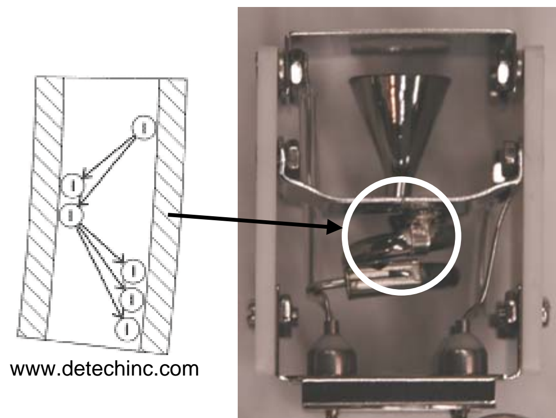

Figure 16. Electron multiplier and schematic.

4.1. TEM experimental failures and the move to the SEM

Early experiments to test the dynamic range of detectors were attempted in a Transmission Electron Microscope (TEM). The purpose of doing this was to mimic the final type of machine which could be used for the DEV. After numerous unsuccessful attempts to test in the TEM using a special sample holder containing a Faraday cup, it was decided that the SEM offered a far more flexible test bed. The failures of the TEM were mainly of two types. First, the very limited locations and feedthroughs available made developing custom detection equipment extremely difficult. Second, to test the dynamic attributes of the detector, scanning of the beam was going to be the first, and ultimately only, mode used to create a time varying current. While there are some limited scanning capabilities on the STEM, they were not nearly as flexible as those in the SEM. The move to the SEM also simplified the experimental flexibility by providing; images of our detector for alignment purposes, area and line scanning capability, 25-

pin feedthroughs for signal attachment, and plenty of room for the detector and any associated hardware. The SEM also offered all of the attributes desired in a DEV system with beam electron objective lenses to focus the beam to a small spot and scanning capability of the spot. Additionally, the source used was a field emission gun, the type typically used for electron holography due to high brightness and good coherence. This last point was not strictly necessary for these experiments as the coherence of the beam was not used. Figure 17 shows the Zeiss Supra 55VP SEM used for the experiments covered in this section.

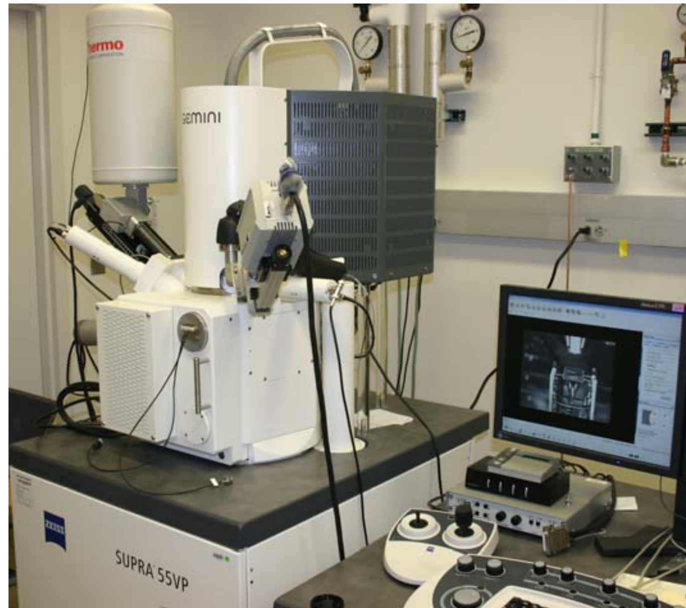

Figure 17. Zeiss Supra 55VP SEM used for the experiments.

4.2. SEM Testing of the Faraday Cup

By far the simplest detector available is the Faraday cup. We used two different cups. The first one was a commercial cup supplied with the SEM for measuring beam current. This consists of a platinum plate with a ~ 50-µm hole as shown in Figure 18. All beam current measurements quoted in this report were made with this device. The cup measures the current by absorbing as many of the electrons as possible including both primary and secondary electrons. After using the commercial cup, which displayed a high level of noise due to the lack of shielding, we developed a shielded wire Faraday measurement device.

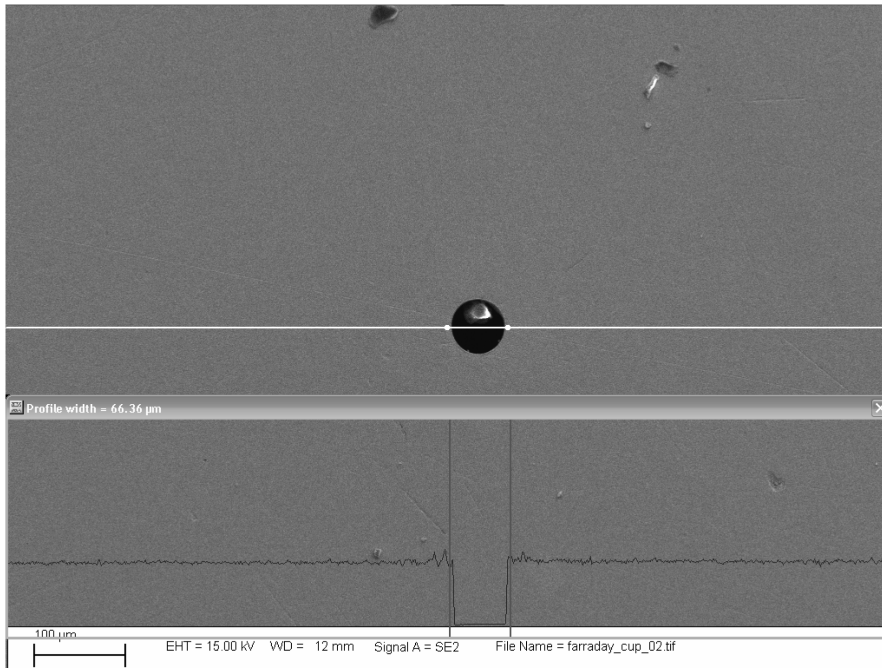

Figure 18. Commercial Faraday cup with 50-µm hole.

For simplicity of construction, we chose to use a simple BNC wire, with the shielding and cladding removed. This was then mounted in a metal cap with a hole filed in the side (see Figure 19). The cap was attached to the shielding of the cable to attempt to reject as much noise as possible. This wire absorbs the incoming electrons and conducts them out of the chamber to the amplifier. Even with good shielding, the Faraday cup proved to have too much noise and not enough gain, yielding an extremely low signal to noise ratio. To some extent, this can be overcome using synchronous detection. This is illustrated in Figure 20. The yellow line in the scope trace is the Faraday wire signal, and the blue line, used for the trigger, is the ET detector signal from the SEM. Note that even with synchronous detection, averaging was required to clean up the signal. The need for averaging and the terrible signal to noise of the Faraday cup, lead to the abandonment of this detector type in favor of the electron multiplier.

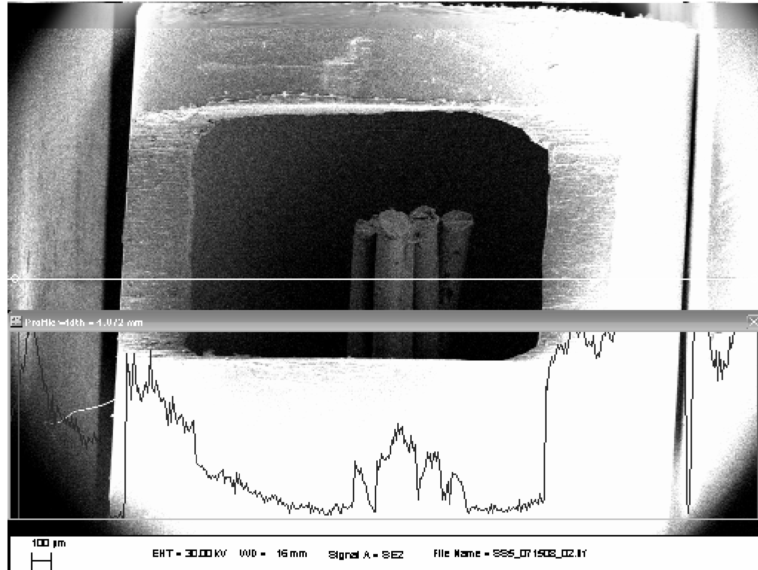

Figure 19. Faraday wire shown in the shielding cup in the SEM.

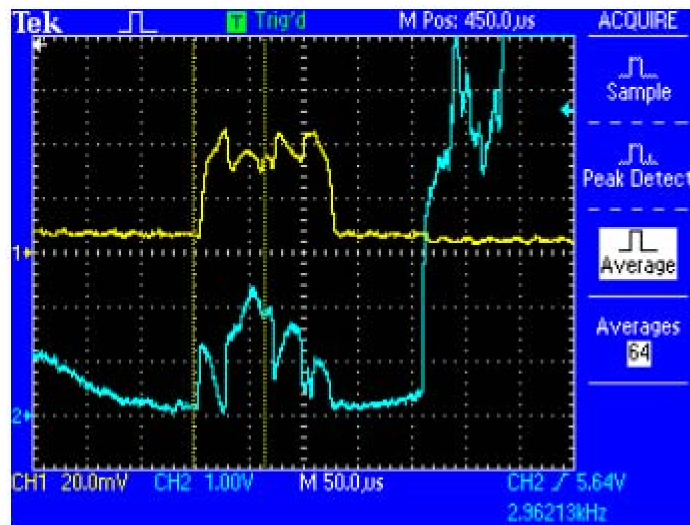

Figure 20. Faraday scope trace (Yellow) and ET detector trace (Blue).

4.3. Electron Multiplier Testing in the SEM

4.3.1 Electron Multiplier and Amplification Circuitry

An electron multiplier (EM) functions by amplifying the number of electrons via secondary electron emission. We obtained an EM from DeTech Inc., custom assembled using one of their standard EM tubes (Figure 16). Note that the Everhardt-Thornley detector uses an EM to amplify the signal, after going through a scintillator and then a photocathode. We decided to cut out the middlemen, and have the electrons go directly into the EM tube. The final EM detector with the grounded shield in place is shown in Figure 21. The shield had an approximately 500 µm hole drilled in the top to allow electrons to enter. This was placed in the microscope on the stage as shown in Figure 22. Figure 23 shows the external equipment used with the EM for making these measurements and included a current amplifier, a high voltage modulation driver, and a high-

voltage power supply. An attempt was made to drive an additional plate on the top of the EM shielding to modulate the acceptance of electrons into the detector. This was successful in rejecting the electrons from the EM, however large noise spikes were created by the driving circuit which made it useless for testing the frequency response of the EM and the idea was abandoned.

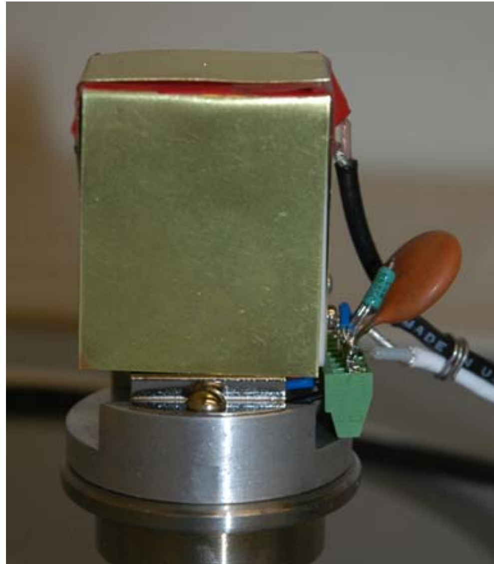

Figure 21. Shielded EM used in the experiments.

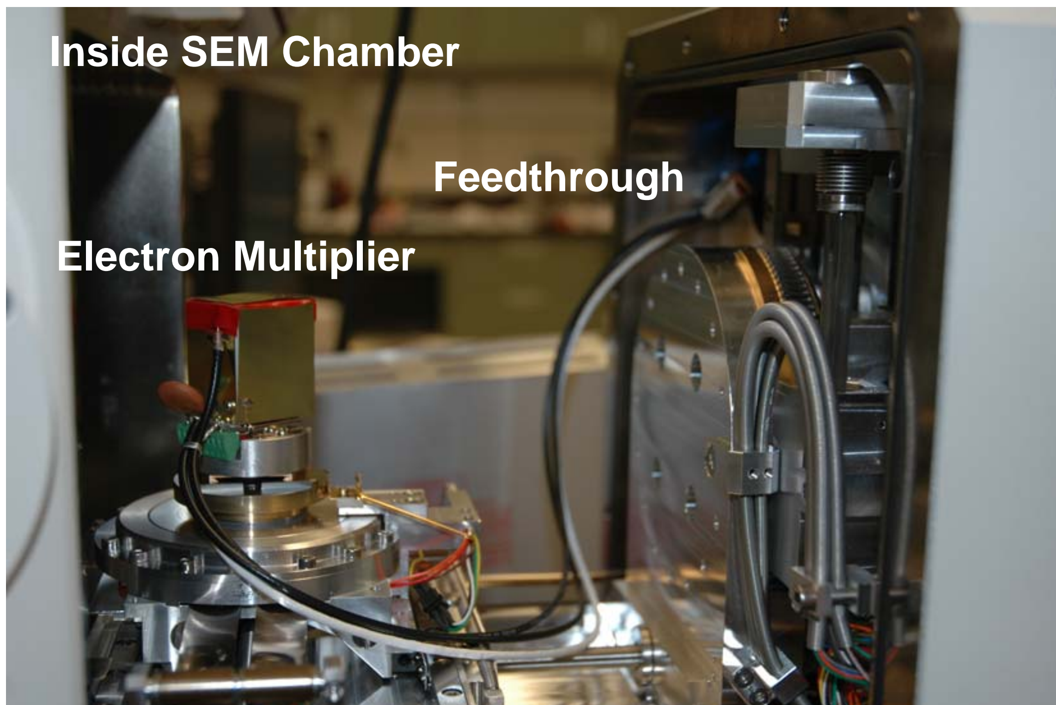

Figure 22. Electron multiplier mounted in SEM chamber.

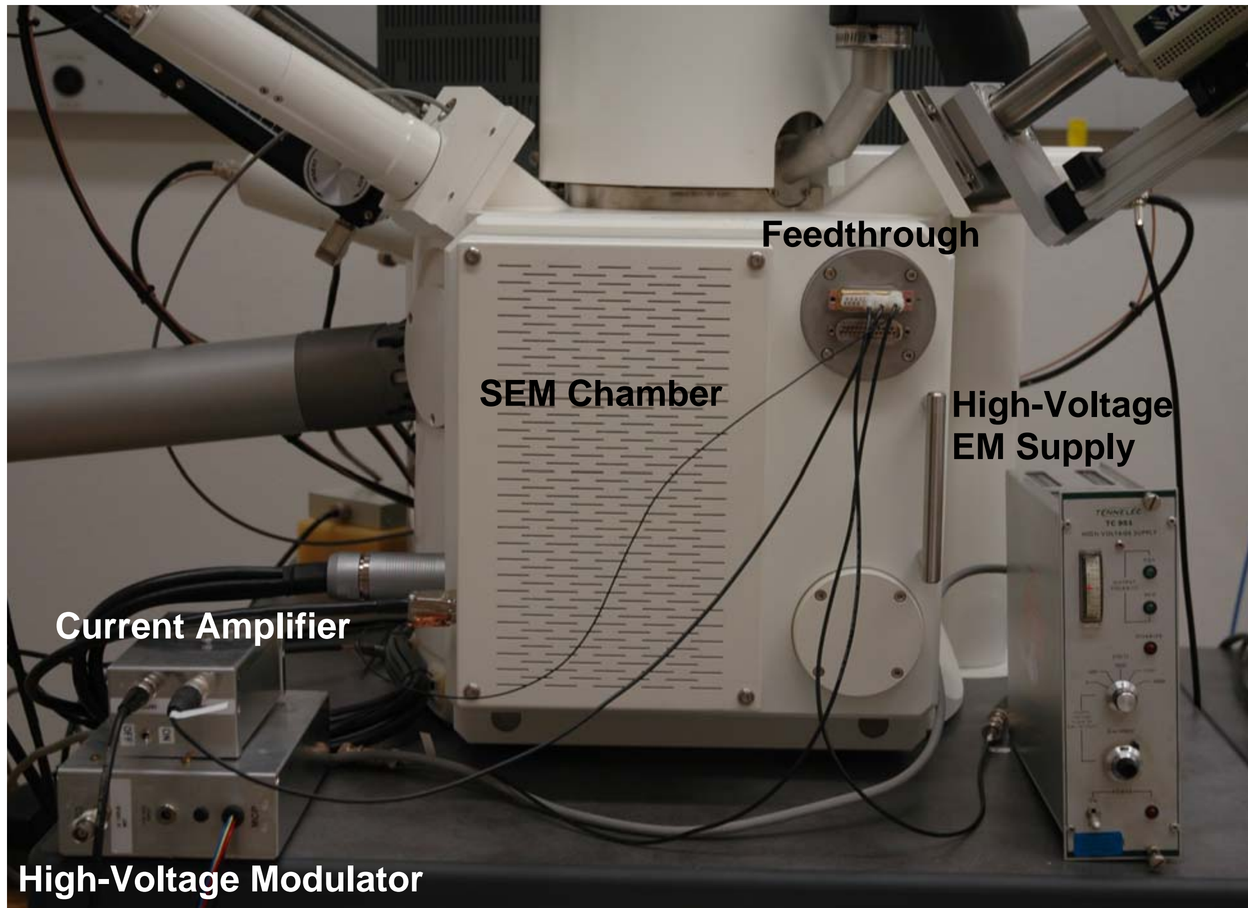

Figure 23. SEM Microscope showing electrical wiring.

The EM was driven by a high voltage power-supply, with voltages between 1200 and 1550 volts. Voltages greater than 1550 were not used as they were likely to cause arcing due to a breakdown in the electrical insulation. The electron multiplier has a variable gain depending on the applied voltage as shown in Figure 24. The incoming electron beam is then amplified and output by the EM as a current. The output was attached to a low-noise transimpedence current amplifier followed by an operational amplifier with a gain of 11. The amplifier schematic is shown in Figure 25. Filter poles are used in both stages to limit the bandwidth to 1-MHz. The overall gain of the current amplifier is 1.1×10^6 volts/ampere. Results for this configuration are discussed in the next section.

While the EM noise was essentially limited by the electron statistics, some noise gain was experienced in the current amplifier due to the cable length between the electron multiplier and the current amplifier. This can be reduced in a future modification by moving the transimpedance amplifier inside the microscope adjacent to the electron multiplier.

Though we expected the temporal response to be flat-topped as the electron beam scanned across the aperture hole, there was significant variation from flat during the transit and it is not clear to us why this is so. A guess would be geometry and secondary electron emission effects as discussed in the next section.

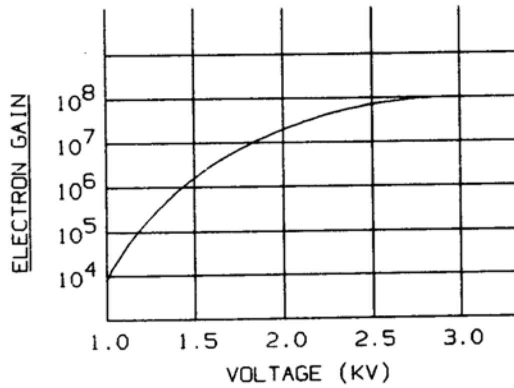

Figure 24. Gain curve for the DeTech electron multiplier (from literature sent with the multiplier).

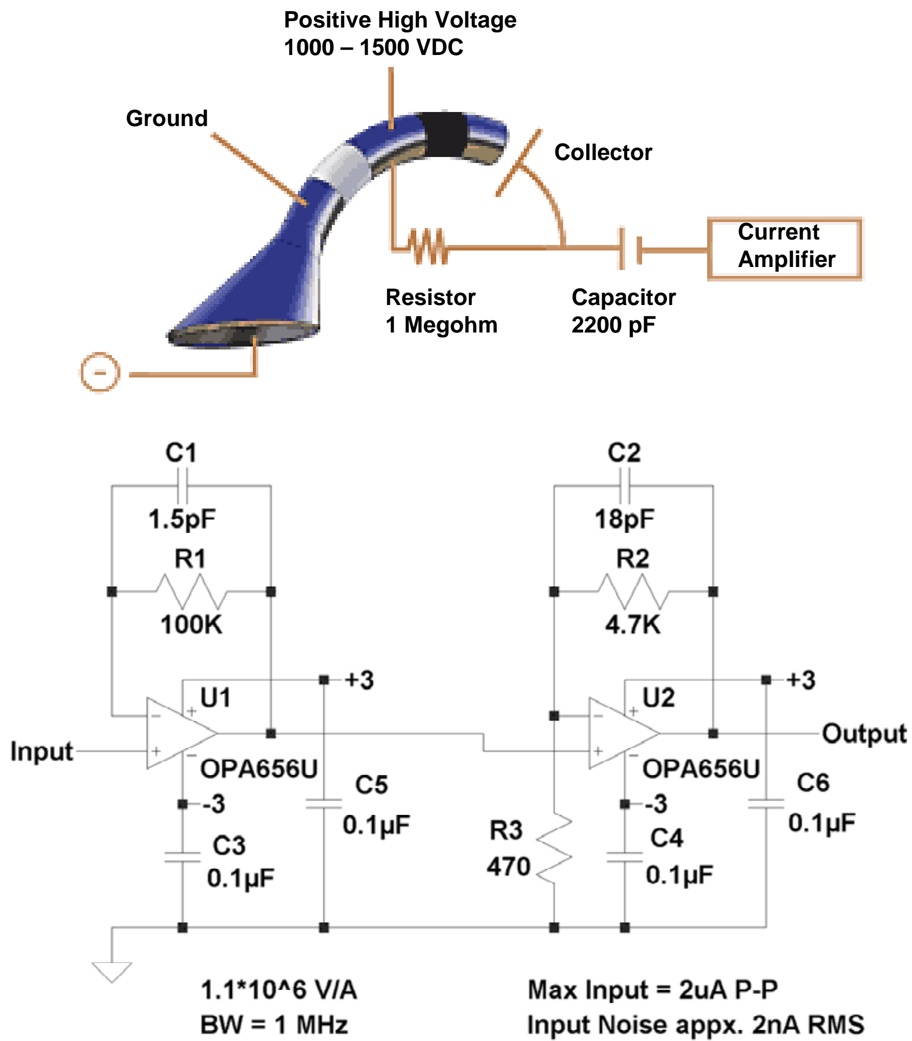

Figure 25. Amplifier schematic.

4.3.2 Electron Multiplier Results

Two tests were conducted using the electron multiplier to ascertain its frequency response and noise level. Initially the frequency response was to be conducted using the EM shielding voltage to modulate the signal at 1 MHz, however, due to the noise inserted into the system by the large voltage applied, this method was abandoned. The inability to use this method had the repercussion of limiting the maximum rise time that could be measured due to the limited scan speeds available in the electron microscope scanning coils. A further complication is that the SEM only reported line scan rates down to Scan Speed 6, with a "zero" scan time reported for Scan Speeds 1-5. The reported time for Scan Speed 6 was 1 ms. Using the SEM reported information from Scan Speeds 6-10, a linear relationship was found for Scan Speed, 1/(repetition rate). It is important to note that the scan repetition is a function of both the scan speed and the scan resolution set on the microscope. For all of the measurements shown in this report, the resolution was set to 512 × 384, rather than the more usual 1024 × 768 to obtain the fastest scan speed possible. Extrapolating from the line created from Scan Speeds 6-10, the repetition rate for Scan Speed 1 is calculated to be 32 kHz. This rate agreed well with the experimental data measured with the EM. These repetition rates can then be used with the scan window size, in millimeters, to calculate the beam scan rate at the sample in meters-per-second. Rates between fractions of a meter-per-second up to 140 m/s were able to be realized with the available equipment.

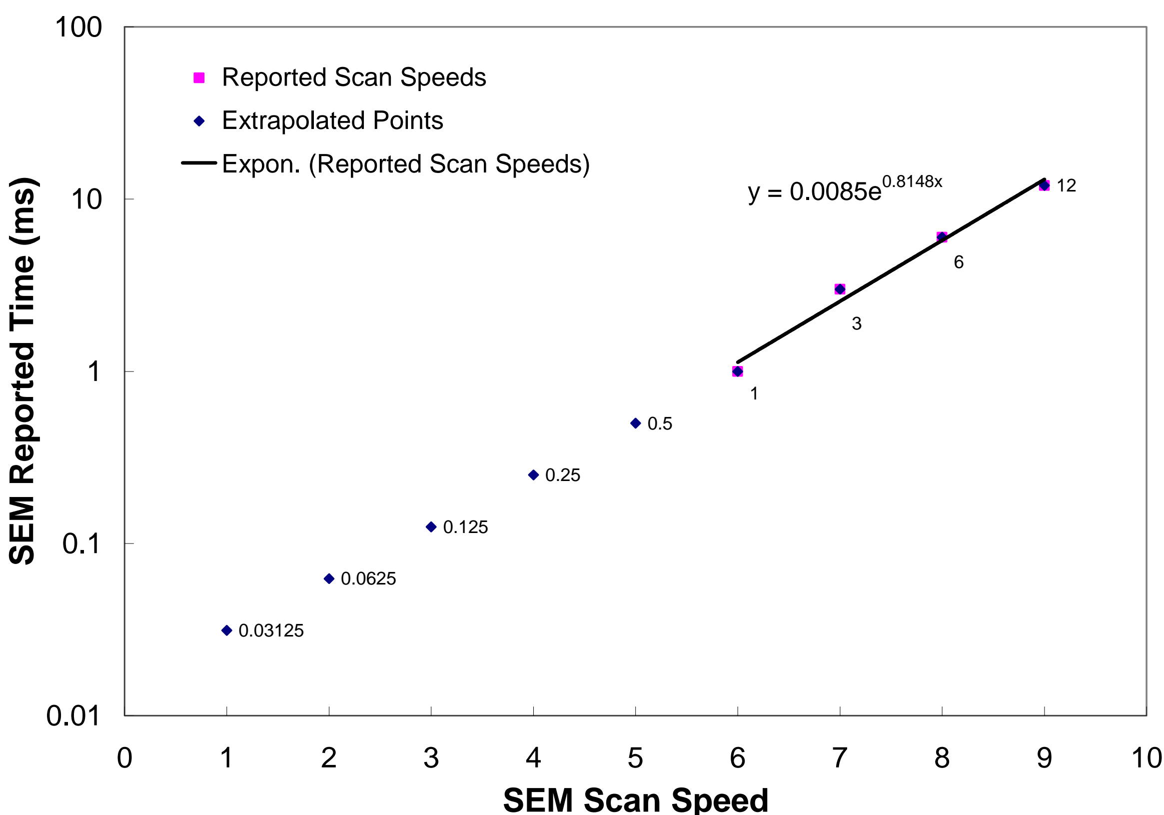

Figure 26. Scan rate versus repetition rate.

The scan rate limitations made it somewhat difficult to demonstrate the desired 1-MHz detection rate. This was mainly due to the effect of the hole geometry and the secondary electron yield of the EM. This is illustrated in Figure 27, which plots the rise time for three different scan rates. As can be seen, with nominally the same trigger-time, different rise times occur for exactly the same beam current. If the hole on the EM had been perfect, and no secondary electrons were emitted, then a perfect step input would have been obtained, however, as can be seen there is a more complex interaction between the beam and the EM acceptance hole. Therefore, for purposes of calculating the maximum rise-time, the fastest scan rate setting was used. The best-case results from the fastest scan rate of 140-m/s demonstrate a bandwidth of 2.5-MHz calculated by finding the rise time of the signal (4-μs) as illustrated in Figure 28. The plot shows four different curves: two of the curves are of a scope average used to remove the noise from the signal and two of the curves are for single-sample acquisitions, at two different gain levels. The gain was set by changing the voltage applied to the EM, for high-gain a voltage of 1440-volts was used, for low gain a voltage of 1400-volts was used. The voltage did not change the rise time, but does however improve the signal-to-noise ratio (SNR).

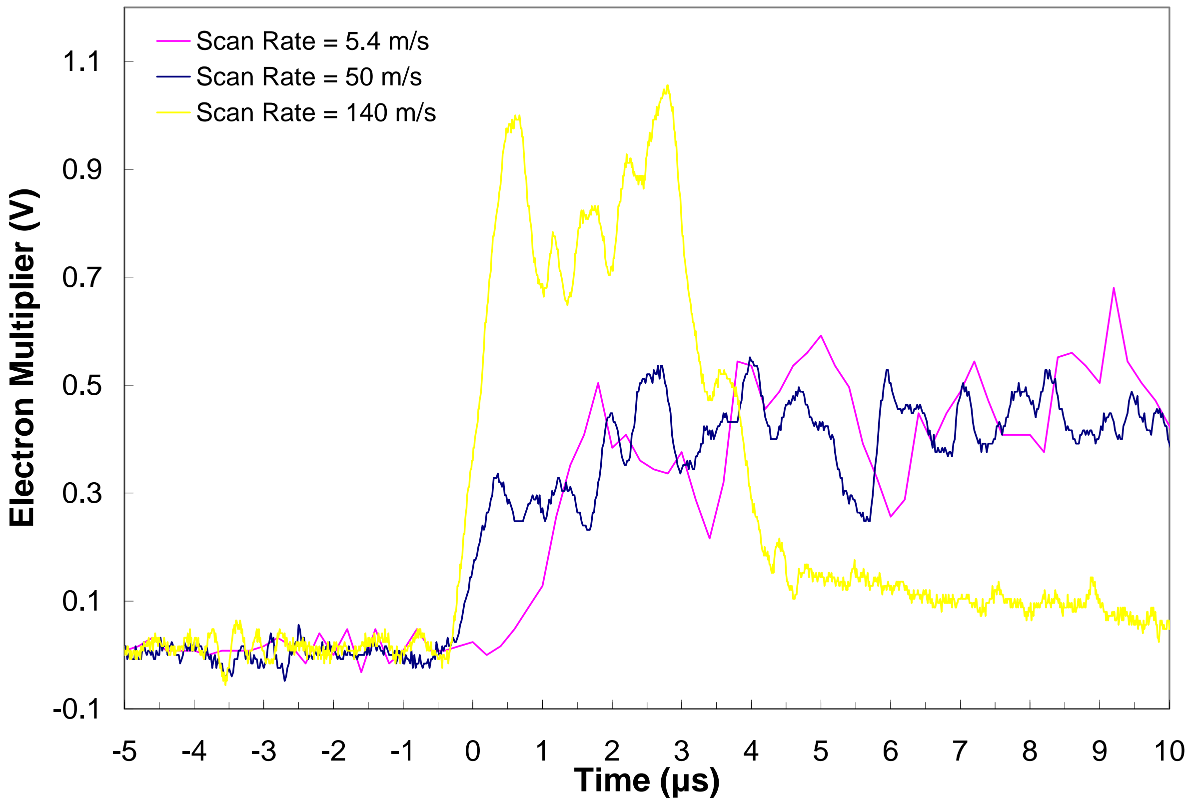

Figure 27. Rise time for different scan rates.

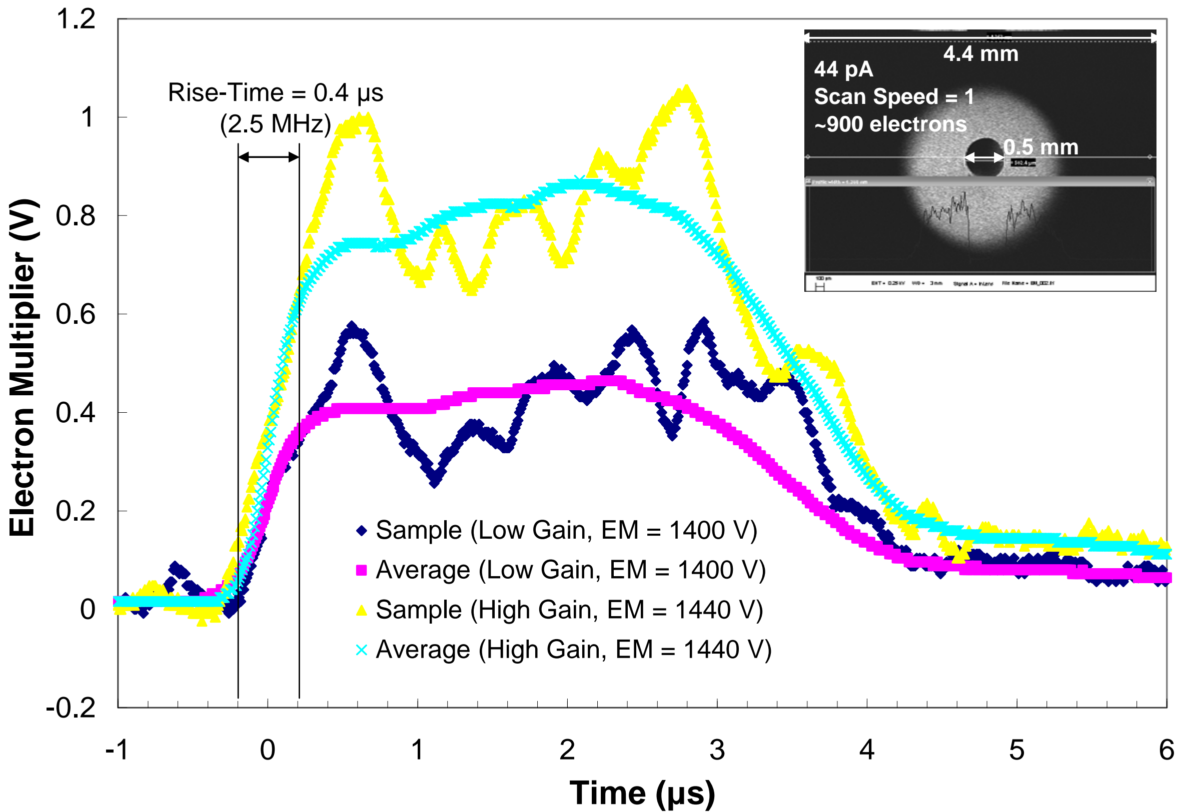

Figure 28. Rise-time experiment showing a 2.5 MHz bandwidth

The SNR was calculated by taking the mean value of the signal during the time it was at its peak, and then calculating the RMS noise during this same time. This is illustrated in Figure 29, which shows the EM response at four different SEM current settings and all with the same scan speed. This resulted in different numbers of electrons entering the hole, from a low of around 400 to a high of 22-thousand electrons. Obviously when the number of electrons for a pulse reaches the level of 400, regardless of the EM gain, the electron statistical noise is going to dominate the signal. However, even with the noisy signal, it is possible to detect when the beam enters and leaves the EM acceptance hole. With rising beam current and greater numbers of electrons-per-second, the SNR level increases as expected as outlined in Table 4.

Table 4. Electron multiplier SNR for different beam currents.

Beam Current (pA)	Number of Electrons	SNR (dB)
315	22,259	22.91
44	3109	15.3
6	424	7.5

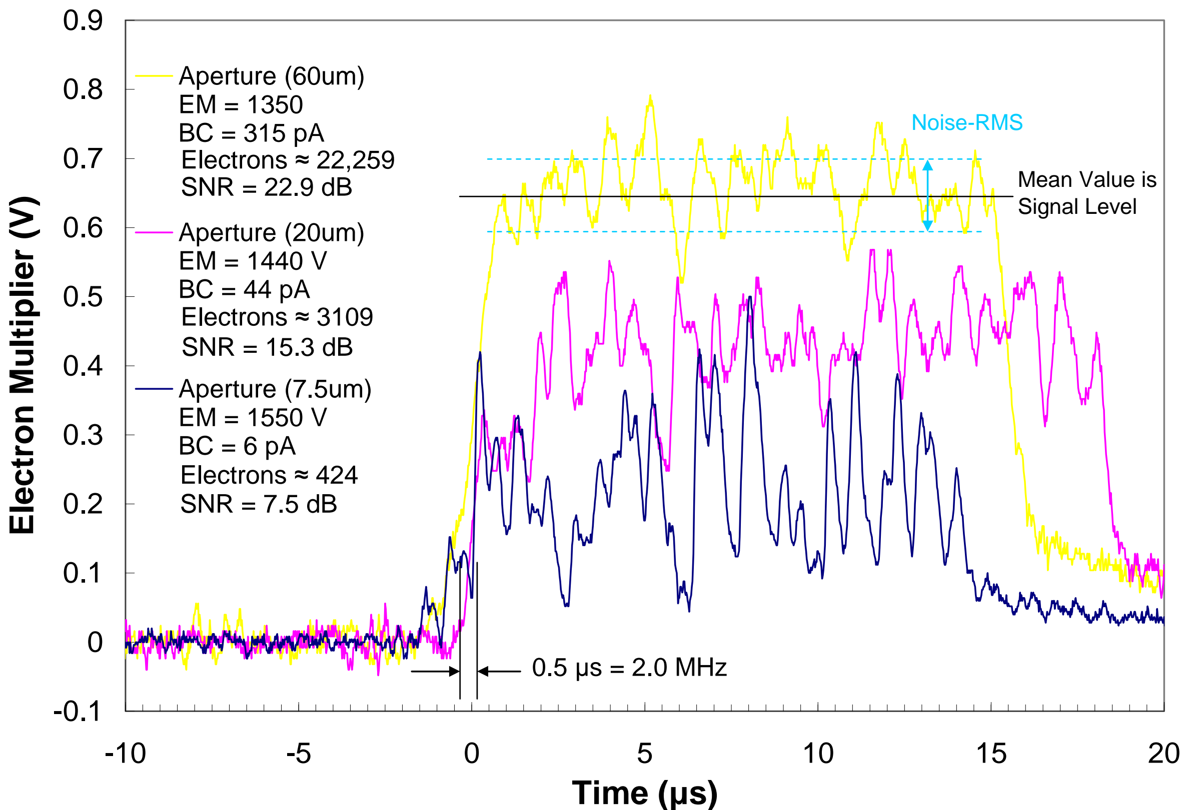

Figure 29. Typical signal response showing the noise levels at different beam currents.

4.4. Evaluation of the EM as a High-Rate Beam Current Detector.

The results of the detector experiments were an unqualified success. We have shown 2-MHz response time with beam currents as low as 44 pA, and maybe down to 6 pA. I have been unable to find any other detectors used in electron microscopes with this type of response times. The Everhardt-Thornley detectors are likely to have similar capabilities, however, the simplicity of the simple EM detector, particularly for the detection of time-varying Doppler beam currents make it an ideal single-point detector for DEV application.

I believe this detector has immediate applications in dynamic nano-scale work, even without the development of the DEV. This detector could be used to measure resonant frequencies and possibly mode-shapes of nano-cantilevers in a scanning electron microscope. The basic setup would be to use the cantilever motion to modulate the beam current as it oscillates with the SEM spot at a stationary point. Some idea of the mode shape could be obtained by looking at the resulting time domain signal.

5. POTENTIAL APPLICATIONS FOR THE DEV

5.2 Applications Introduction

One of the powers of the DEV is that the electron beam, unlike a laser, can be affected by not just the velocity of a surface as in a traditional laser Doppler application, but by a varying magnetic or electric field. Really, anything that changes the phase of the passing electron beam can be a candidate for DEV measurements. This is seen in the following equation given without derivation [16]:

$$\Delta\phi = \frac{1}{\hbar}\oint (mv - eA)dS \ . \tag{5.1}$$

where ϕ is the phase, $\boldsymbol{v}$ is the velocity, $\boldsymbol{A}$ is the electromagnetic field vector potential, $\boldsymbol{S}$ is the integration path containing the area between the object and reference beam and $\hbar$ is Plank's constant divided by 2π. This is an important equation and somewhat difficult to understand. It states that the wavefront is not perpendicular to the direction of momentum, $m\boldsymbol{v}$, as is typically the case, but is perpendicular to the generalized momentum ($m\boldsymbol{v}$ - $e\boldsymbol{A}$), often termed the canonical momentum. Equation (5.1) leads to an ambiguity in the phase calculated when an electron travels through an electromagnetic field because the vector $\boldsymbol{A}$ is not uniquely defined. This is overcome practically by integrating around a closed loop that contains the object beam and the reference beam, as discussed in Section 1.2. The magnetic or electric fields referred to are those contained between the two beams of the interferometer. Equation (5.1) can be simplified with some further math and separated into an electrostatic and magnetic portion:

$$\Delta\phi = \frac{e}{\hbar}\int mv^2 dt - \frac{e}{\hbar}\int BdS = \frac{eLU}{\hbar v} - \frac{e}{\hbar}\oint BdS \ . \tag{5.2}$$

where $\boldsymbol{B}$ is the magnetic field, U is the electric field, and L is the distance traveled through the field. The first portion of the equation is the effect of the electric field on the phase and the second contains the effect of the magnetic field. This equation does not, however, include the energy shift due to inelastic scattering off of a moving surface which is the first topic I will address.

5.2. Mechanical Motion

Mechanical motion of an object is the first type of motion traditionally associated with Doppler. In an electron microscope it works by setting up a beam splitting interferometer and reflecting a portion of the beam onto the sample, which reflects it back to be recombined to create the moving fringes. The object in this arrangement is functioning as an electron mirror. An electron mirror can be created if the surface of the object is conducting, and held at a potential. In front of the mirror is another electrode which causes the electrons to reverse direction after reaching the surface of the object. With the DEV setup in this configuration, the resulting Doppler frequency is:

$$f_D = \frac{d\phi}{dt} = \frac{4\Delta v}{3\lambda}, \tag{5.3}$$

where f_D is the Doppler frequency in Hz, $d\phi/dt$ is the instantaneous rate of phase change, Δv is the velocity difference between the object and reference leg of the interferometer. Using this relation and varying the electron energy, an idea of the range of velocities able to be measured can be determined as shown in Table 5.

5.3. Varying electric fields

The electric field applies a force to the passing electrons which changes the phase of the reference leg in relation to the object leg according to Equation (5.2). This arrangement has been used typically to measure either a samples thickness or its mean inner potential. Other examples have used the phase shift to measure the coherence length of an electron beam by changing the applied field until loss of fringe contrast occurs indicating a phase shift greater than the coherence length has occurred [19]. Of course, if the electric field is time-varying, a time varying phase shift, or Doppler frequency will result according to the following equation:

$$f_D = \frac{d(\Delta\phi)}{dt} = \frac{eL}{\hbar v}\frac{dU}{dt}, \qquad (5.4)$$

where U is the potential difference between the object and reference beams, v is the group velocity and L is the distance the beam travels through the electric field. Table 5 shows the measurable field changes in kV/s for a 1 MHz bandwidth DEV. Because the Doppler frequency depends on the velocity of the electron through the field, the sensitivity of the DEV can be varied by changing the electron velocity, controlled by the accelerating potential of the microscope. That is, by using a low energy electron beam (slow electrons) greater sensitivity to the electric field is obtained.

5.4. Varying magnetic fields

Another quantity that can be measured is the magnetic field. This property has already been exploited in electron holography to measure static and quasi-static magnetic fields in various materials [5]. The equation simplified from above relates the magnetic field to the Doppler frequency by:

$$f_D = \frac{d(\Delta\phi)}{dt} = \frac{eL}{\hbar}\frac{d\Phi_m}{dt}, \qquad (5.5)$$

where $d\Phi_m/dt$ is the time varying rate of the magnetic field change in Webers/s contained between the object and reference beams. Interestingly, the phase change only depends on the path and the magnetic flux and is not related to the electron beam energy.

Table 5. Dynamic rates for a 1-MHz sampling capability

TEM Parameters			Measured Properties		
Source Acc. (kV or keV)	electron λ (nm)	electron v (m/s)	Δv (μm/s)	dU/dt (kV/s)	dφ/dt (Wb/s)
0.01	0.38783	1.88E+06	290.87	1	6.58E-10
0.1	0.12264	5.93E+06	91.98	4	6.58E-10
10	0.01220	5.85E+07	9.15	38	6.58E-10
100	0.00370	1.64E+08	2.78	108	6.58E-10
200	0.00251	2.08E+08	1.88	137	6.58E-10
1000	0.00087	2.82E+08	0.65	186	6.58E-10

6. CONCLUSIONS

6.1. Possible DEV Configurations and Applications

It is shown in Section 3.1 that the basic electron holography setup with a reference grating might be practical for DEV. However, interaction with the object specimen is not spatially defined. This geometry works well for object phase changes uniformly across the object, but not when phase varies across the object.

Instead, Leuthner's STEM system [20] shown in Figure 30 may be more practical for obtaining DEV signals as a function of position on the object specimen. Although not designed as a DEV system, it is easily adapted. Instead of detecting phase at each scan point, the dwell time can be increased and the PMT electrical signal can be analyzed by taking the Fourier transform of temporally sampled signals. The average square of these Fourier transforms will correspond to the power spectrum of the DEV signal. The spot size of this STEM-like system using modern equipment should be similar to the 0.2 nm spot size achieved with the Isakozawa *et al.* system [21]. However, the reference grating required in the Leunthner-like system might be problematic. For example, the grating design influences signal quality. In addition, gratings might be useful over only a limited range of electron voltages.

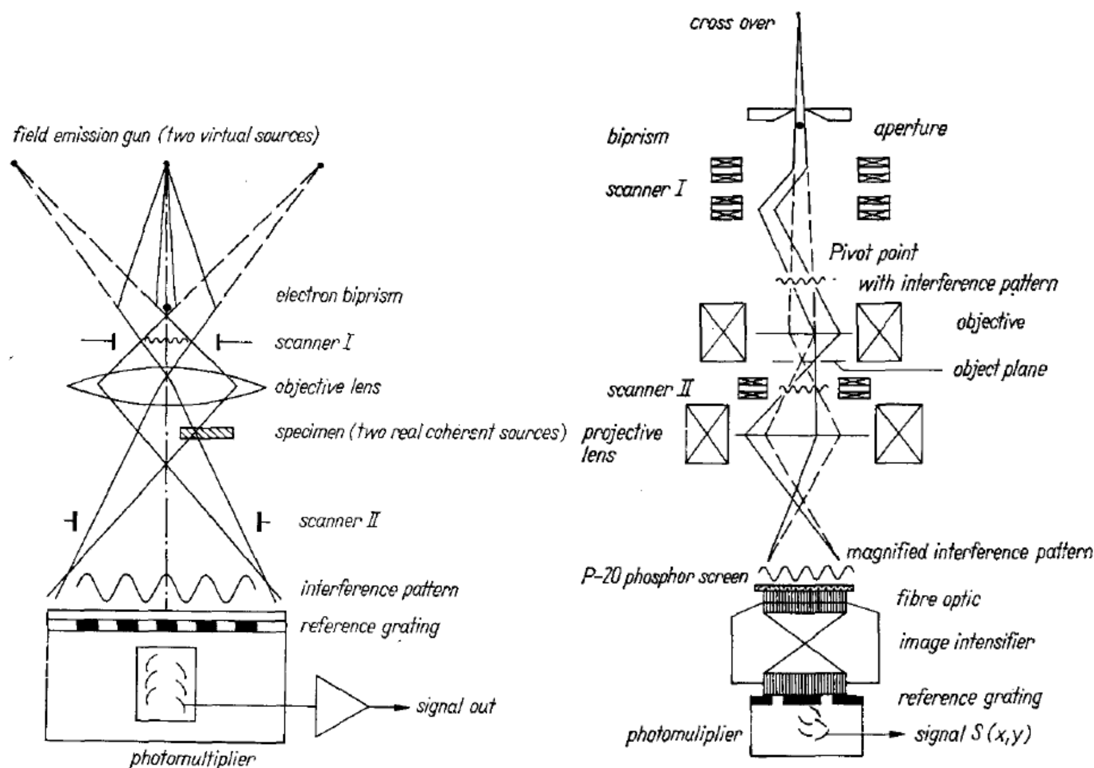

Figure 30. STEM Holography. (a) Conceptual diagram; and (b) Experimental setup [20].

Instead of using a reference grating, the Mach-Zehnder-like concept shown in Figure 31 might provide a more convenient arrangement. In this system, a converging electron beam focuses onto the sample. Because the beam is split by Grating 1, a complementary beam is focused into the reference path. The object and reference beams are recombined by the second electron biprism. At this point, interference occurs, but the fringe spatial frequency will probably be too high to be

detected. Grating 2 is used to heterodyne the combined pattern into a zero-order beam. After Grating 2, electron optics reimage the test object onto a detector plane. Because each point in the object path is conjugate to a point in the reference path, an interference image is generated directly on the detector plane, that is a Linnik-type configuration. If a sufficiently fast imaging detector is available, a DEV signal image could be directly detected. More likely is that a fast point detector will need to be scanned across the image plane in order to obtain a DEV signal. A scanner element system could be incorporated, like in the Leunthner system, in order to avoid having to scan the detector. For low-energy electrons (< a few keV), gratings are a practical alternative for the beam splitter elements. For example, transmission characteristics of transmission gratings used with low-energy (0.5 keV) electrons has been discussed by McMorran [22]. For higher-energy electrons, periodic crystals may be a better choice.

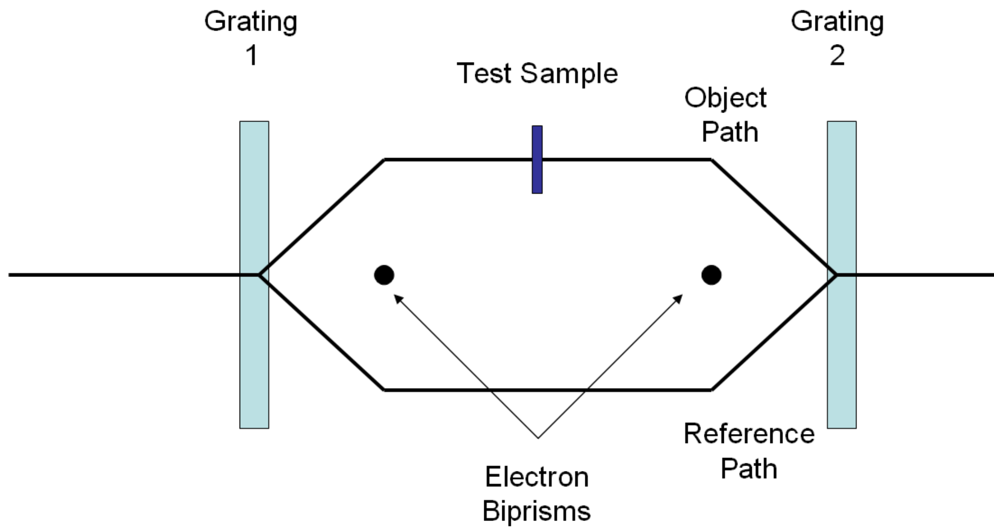

Figure 31. Conceptual arrangement of a Mach-Zehnder-like STEM DEV device.

The system concept shown in Figure 10 is similar to an optical Linnik microscope. A full analysis of the Linnik microscope is given in Appendix A. Although the optical Linnik microscope is reasonably straightforward to use, a primary difficulty is alignment of the beam paths. They must be matched so that the point spread functions of each path overlap in the detection plane for good fringe contrast. In this respect, the Linnik configuration exhibits different coherence properties than the basic electron holography setup. It is not necessary to use a coherent source with the Linnik configuration.

7. REFERENCES

1. Reu, P.L., *Development of the Doppler electron velocimeter: theory*. 2007, Sandia National Laboratory.
2. Reu, P.L. *Doppler Electron Velocimeter-a Proposed Nano-scale Dynamic Measurement System*. in *Society of Experimental Mechanics*. 2007. Springfield, MA: SEM.
3. Lichte, H. and M. Lehmann, *Electron holography - basics and applications.* Reports on Progress in Physics, 2008. **71**(1): p. -.
4. Joy, D.C., et al., *Practical Aspects of Electron Holography.* Ultramicroscopy, 1993. **51**(1-4): p. 1-14.
5. Tonomura, A., *Electron Holography*. 2nd ed. 1999, New York: Springer.
6. Tonomura, A. 9/25/2008; Available from: <http://www.hqrd.hitachi.co.jp/em/movie.cfm>.
7. Feynman, R.P., R.B. Leighton, and M. Sands, *The Feynman Lectures on Physics*. 1977, Menlo Park, CA: Addison-Wesley Publishing Co.
8. Silverman, M.P., *On the Feasibility of Observing Electron Antibunching in a Field-Emission Beam.* Physics Letters A, 1987. **120**(9): p. 442-446.
9. Spence, J.C.H., W. Qian, and M.P. Silverman, *Electron Source Brightness and Degeneracy from Fresnel Fringes in-Field Emission Point Projection Microscopy.* Journal of Vacuum Science & Technology a-Vacuum Surfaces and Films, 1994. **12**(2): p. 542-547.
10. Spence, J.C.H. and M.R. Howells, *Synchrotron soft X-ray and field-emission electron sources: a comparison.* Ultramicroscopy, 2002. **93**(3-4): p. 213-222.
11. Young, T., *The Bakerian Lecture: On the Theory of Light and Colours.* Philosophical Transactions of the Royal Society of Londong, 1802. **92**(1802): p. 12-48.
12. Born, M. and E. Wolf, *Principles of Optics*. 7th ed. 1999, Cambridge: Cambridge University Press.
13. Shatten, H. and J. Pawley, *Biological Low-Voltage Scanning Electron Microscopy*. 2008, New York: Springer.
14. Abdulhalim, I., *Competence between spatial and temporal coherence in full field optical coherence tomography and interference microscopy.* Journal of Optics a-Pure and Applied Optics, 2006. **8**(11): p. 952-958.
15. Herring, R.A., et al., *Interferometry Using Convergent Electron Diffracted Beams Plus an Electron Biprism (Cbed+Ebi).* Ultramicroscopy, 1995. **60**(1): p. 153-169.
16. Völkl, E., L.F. Allard, and D.C. Joy, eds. *Introduction to Electron Holography*. 1999, Kluwer Academic/Plenum Publishers: New York.
17. Goldstein, J., et al., *Scanning Electron Microscopy and X-Ray Microanalysis*. Vol. 3rd. 2003, New York: Kluwer Academic/Plenum Publishers.
18. Reimer, L., *Transmission Electron Microscopy*. 3rd ed. 1993, New York: Springer-Verlag.
19. Schmid, H., *Coherence Length Measurement by Producing Extremely High Phase Shifts*, in *European Conference on Electron Microscopy*. 1984: Budapest.
20. Leuthner, T., H. Lichte, and K.H. Herrmann, *STEM-HOLOGRAPHY USING THE ELECTRON BIPRISM.* Physica Status Solidi a-Applied Research, 1989. **116**(1): p. 113-121.

21. Isakozawa, S., et al., *The development and characteristics of a high-speed EELS mapping system for a dedicated STEM.* Journal of Electron Microscopy, 2008. **57**(2): p. 41-45.
22. McMorran, B., et al., *Diffraction of 0.5 keV electrons from free-standing transmission gratings.* Ultramicroscopy, 2006. **106**(4-5): p. 356-364.

APPENDIX A: THOERETICAL DEVELOPMENT FOR PARTIALLY COHERENT LINNIK SYSTEM

This appendix is from Tom Milster, University of Arizona, delivered as part of his contract with Sandia National Laboratories.

A.1 Imaging in each path

From Eq. (A.24) of the July 25, 2008 report,, coherent imaging in each path is governed by

$$\begin{aligned} U(x_0, y_0) &= \frac{1}{|m_T|} e^{jk(r+r')} U_{z=0}\left(\frac{x_0}{m_T}, \frac{y_0}{m_T}\right) ** \mathbf{F}_{y_0}^{-1}\mathbf{F}_{x_0}^{-1}\left\{T(m_T\xi', m_T\eta')\exp\left[j2\pi W(\xi', \eta')\right]\right\} \\ &= \frac{1}{|m_T|} e^{jk(r+r')} U_{z=0}\left(\frac{x_0}{m_T}, \frac{y_0}{m_T}\right) ** h(x_0, y_0) \quad , \end{aligned} \tag{A.1}$$

where low numerical aperture is assumed for both object and image spaces,[2] (x_0, y_0) are coordinates of the image plane, (ξ', η') are spatial frequencies associated with the exit pupil, m_T is transverse magnification of the path, $T(m_T\xi', m_T\eta')$ is the transmission of the entrance pupil scaled to the exit pupil, $W(\xi', \eta')$ is the aberration function in units of waves, $(x_p' = \lambda r'\xi', y_p' = \lambda r'\eta')$ are coordinates on the exit pupil reference sphere with radius r', and $h(x_0, y_0)$ is the coherent point spread function. Note that Eq. (A.1) describes propagation for each coherent field component emitted by the source. Each path is linear and shift invariant.

The aberration function $W(\xi', \eta')$ accounts for displacement (Δ_x, Δ_y) of the image point in the observation plane and axial defocus Δ_z. Other aberration terms due to spherical aberration astigmatism, etc., are included in an additional term $w(\xi', \eta')$. We assume that displacements Δ_x, Δ_y and Δ_z are small compared to r'. The aberration function is given by

$$W(\xi', \eta') = \xi'\Delta_x + \eta'\Delta_y + W_z \bullet \left(\xi'^2 + \eta'^2\right) + w(\xi', \eta'), \tag{A.2}$$

where

$$W_z = \frac{\Delta_z / r'}{r' + \Delta_z} \tag{A.3}$$

---

[2] For low numerical aperture, $\sqrt{\frac{\gamma}{\gamma'}} \approx 1$.

A.2 The coherence function and fringe visibility

Following the development of Hopkins,[2] we know that irradiance in the observation plane is given by

$$I_{total}(x_0, y_0; \tau) = I_1(x_0, y_0) + I_2(x_0, y_0) + 2\sqrt{I_1(x_0, y_0) I_2(x_0, y_0)}\,\mathrm{Re}\left[\gamma_{12}(\tau)\right], \quad \text{(A.4)}$$

where I_1 and I_2 are the irradiances at the observation point from the test (1) and reference (2) paths, τ is the propagation delay between the reference and test paths, and $\gamma_{12}(\tau)$ is the normalized mutual coherence function given by[3]

$$\gamma_{12}(\tau) = \frac{\left\langle U_1(x_0, y_0; t) U_2^*(x_0, y_0; t+\tau)\right\rangle}{\sqrt{I_1(x_0, y_0) I_2(x_0, y_0)}}. \quad \text{(A.5)}$$

We assume that the paths are reasonably well matched, so τ is small compared to the source's inverse bandwidth. In this case, the approximation $\tau = 0$ is a reasonable assumption. Additionally, we assume that irradiance differences in the observation plane are small with respect to $I_1(x_0, y_0)$ and $I_2(x_0, y_0)$, so if

$$I_1(x_0, y_0) \approx I_2(x_0, y_0), \quad \text{(A.6)}$$

then

$$I_{total}(x_0, y_0; 0) \approx 2 I_1(x_0, y_0)\left\{1 + \mathrm{Re}\left[\gamma_{12}(0)\right]\right\}. \quad \text{(A.7)}$$

Fringe contrast, found by using Eq. (A.7), is

$$V = \frac{\left[I_{total}\right]_{\max} - \left[I_{total}\right]_{\min}}{\left[I_{total}\right]_{\max} + \left[I_{total}\right]_{\min}} \approx \left|\gamma_{12}(0)\right|. \quad \text{(A.8)}$$

With $\tau = 0$ and application of Eq. (A.6), Eq. (A.5) becomes

$$\gamma_{12}(0) = \frac{\left\langle U_1(x_0, y_0; t) U_2^*(x_0, y_0; t)\right\rangle}{I_1(x_0, y_0)} = \frac{J_{12}(x_0, y_0)}{I_1(x_0, y_0)}, \quad \text{(A.9)}$$

where $J_{12}(x_0, y_0)$ is the mutual intensity at the observation plane. Use of Eq. (A.1) to describe the fields at the observation plane for each path yields

---

[3] $\langle\ \rangle$ denotes time average.

$$J_{12}(x_0,y_0)=\frac{1}{|m_T|^2}\left\langle\left[U_{z_1=0}\left(\frac{x_0}{m_T},\frac{y_0}{m_T}\right)**h_{10}(x_0,y_0)\right]\left[U^*_{z_2=0}\left(\frac{x_0}{m_T},\frac{y_0}{m_T}\right)**h^*_{20}(x_0,y_0)\right]\right\rangle$$
$$=\int_{-\infty}^{\infty}\int_{-\infty}^{\infty}\int_{-\infty}^{\infty}\int_{-\infty}^{\infty}\left\langle U_{z_1=0}\left(\frac{u}{m_T},\frac{v}{m_T}\right)U^*_{z_2=0}\left(\frac{u'}{m_T},\frac{v'}{m_T}\right)\right\rangle$$
$$\times h_{10}(x_0-u,y_0-v)h^*_{20}(x_0-u',y_0-v')dudvdu'dv'$$
$$=\int_{-\infty}^{\infty}\int_{-\infty}^{\infty}\int_{-\infty}^{\infty}\int_{-\infty}^{\infty}J_{z_{12}=0}\left(\frac{u}{m_T},\frac{v}{m_T},\frac{u'}{m_T},\frac{v'}{m_T}\right)h_{10}(x_0-u,y_0-v)h^*_{20}(x_0-u',y_0-v')dudvdu'dv' \quad . \tag{A.10}$$

The term $J_{z_{12}=0}(x_1,y_1,x_2,y_2)$ describes an effective mutual intensity reflected from the test and reference surfaces. To continue the analytical framework, $J_{z_{12}=0}(x_1,y_1,x_2,y_2)$ is further decomposed into elements describing propagation from the illumination pupil to the reference and test surfaces. That is,

$$J_{z_{12}=0}(x_1,y_1,x_2,y_2)=\int_{-\infty}^{\infty}\int_{-\infty}^{\infty}\int_{-\infty}^{\infty}\int_{-\infty}^{\infty}\left\langle U_i\left(\frac{u}{m_{Ti}},\frac{v}{m_{Ti}}\right)U^*_i\left(\frac{u'}{m_{Ti}},\frac{v'}{m_{Ti}}\right)\right\rangle$$
$$\times h_{i1}(x_1-u,y_1-v)h^*_{i2}(x_2-u',y_2-v')dudvdu'dv'$$
$$=\int_{-\infty}^{\infty}\int_{-\infty}^{\infty}\int_{-\infty}^{\infty}\int_{-\infty}^{\infty}J_i\left(\frac{u}{m_{Ti}},\frac{v}{m_{Ti}},\frac{u'}{m_{Ti}},\frac{v'}{m_{Ti}}\right)$$
$$\times h_{i1}(x_1-u,y_1-v)h^*_{i2}(x_2-u',y_2-v')dudvdu'dv' \quad , \tag{A.11}$$

where m_{Ti} is the transverse magnification between the illumination pupil and the reference and test surfaces, $J_i(x_i,y_i,x'_i,y'_i)$ is the mutual intensity at the illumination pupil, and h_{i1} and h_{i2} describe the coherent point spread functions to the reference and test surfaces from the illumination pupil.

Finally, $J_i(x_i,y_i,x'_i,y'_i)$ is decomposed into elements describing propagation from the source to the illumination pupil. That is,

$$J_i(x_i,y_i,x'_i,y'_i)=\int_{-\infty}^{\infty}\int_{-\infty}^{\infty}\int_{-\infty}^{\infty}\int_{-\infty}^{\infty}\left\langle U_s\left(\frac{u}{m_{Ts}},\frac{v}{m_{Ts}}\right)U^*_s\left(\frac{u'}{m_{Ts}},\frac{v'}{m_{Ts}}\right)\right\rangle$$
$$\times h_{si}(x_i-u,y_i-v)h^*_{si}(x'_i-u',y'-v'_i)dudvdu'dv' \tag{A.12}$$
$$=\int_{-\infty}^{\infty}\int_{-\infty}^{\infty}M\left(\frac{u}{m_{Ts}},\frac{v}{m_{Ts}}\right)h_{si}(x_i-u,y_i-v)h^*_{si}(x'_i-u,y'-v)dudv \quad ,$$

where m_{Ts} is the transverse magnification of the source to the illumination pupil, h_{si} is the associated point spread function, and $M\left(x_s, y_s\right)$ is the radiant exitance (in units of Wm^{-2}) of the quasi-monochromatic source distribution.

A.3 Incoherent illumination pupil (Critical illumination)

If the illumination pupil is illuminated incoherently with the source directly in the pupil,

$$J_i\left(x_i, y_i, x_i', y_i'\right) = \kappa M\left(x_i, y_i\right)\delta\left(x_i - x_i', y_i - y_i'\right) \ , \tag{A.13}$$

where κ is a constant chosen to assure proper volume of $J_i\left(x_i, y_i, x_i', y_i'\right)$ as defined by Goodman,[4] where

$$\kappa = \frac{\left(\bar{\lambda}\right)^2}{\pi} \ . \tag{A.14}$$

Effective mutual intensity between the reference and test surfaces now becomes

$$\begin{aligned} J_{z_{12}=0}(x_1, y_1, x_2, y_2) &= \frac{\kappa}{\left|m_{Ti}\right|^2}\int_{-\infty}^{\infty}\int_{-\infty}^{\infty}\int_{-\infty}^{\infty}\int_{-\infty}^{\infty} M\left(\frac{u}{m_{Ti}}, \frac{v}{m_{Ti}}\right)\delta\left(\frac{u-u'}{m_{Ti}}, \frac{v-v'}{m_{Ti}}\right) \\ &\quad \times h_{i1}\left(x_1 - u, y_1 - v\right)h_{i2}^*\left(x_2 - u', y_2 - v'\right)du\,dv\,du'\,dv' \\ &= \kappa\int_{-\infty}^{\infty}\int_{-\infty}^{\infty} M\left(\frac{u}{m_{Ti}}, \frac{v}{m_{Ti}}\right)h_{i1}\left(x_1 - u, y_1 - v\right)h_{i2}^*\left(x_2 - u, y_2 - v\right)du\,dv \ . \end{aligned} \tag{A.15}$$

Combination of Eq. (A.15) with Eq. (A.10) yields

[4] J. Goodman, Statistical Optics, (John Wiley and Sons, Inc., New York, 1985)

$$J_{12}(x_0,y_0)=\int_{-\infty}^{\infty}\int_{-\infty}^{\infty}\int_{-\infty}^{\infty}\int_{-\infty}^{\infty}\left[\kappa\int_{-\infty}^{\infty}\int_{-\infty}^{\infty}M\left(\frac{u}{m_{Ti}},\frac{v}{m_{Ti}}\right)h_{i1}\left(\frac{u''}{m_T}-u,\frac{v''}{m_T}-v\right)h_{i2}^*\left(\frac{u'}{m_T}-u,\frac{v'}{m_T}-v\right)\right]dudv$$
$$\times\, h_{10}(x_0-u'',y_0-v'')h_{20}^*(x_0-u',y_0-v')\,du''dv''du'dv'$$
$$=\kappa\int_{-\infty}^{\infty}\int_{-\infty}^{\infty}M\left(\frac{u}{m_{Ti}},\frac{v}{m_{Ti}}\right)$$
$$\times\left[\begin{array}{l}\int_{-\infty}^{\infty}\int_{-\infty}^{\infty}h_{i1}\left(\frac{u''}{m_T}-u,\frac{v''}{m_T}-v\right)h_{10}(x_0-u'',y_0-v'')\,du''dv''\\ \qquad\times\int_{-\infty}^{\infty}\int_{-\infty}^{\infty}h_{i2}^*\left(\frac{u'}{m_T}-u,\frac{v'}{m_T}-v\right)h_{20}^*(x_0-u',y_0-v')\,du'dv'\end{array}\right]dudv \qquad \text{(A.16)}$$

Although Eq. (A.16) appears ominous, it can be significantly simplified. First, we analyze only the first integral inside the brackets that pertains to the test path (1). Coherent point spread functions from test and reference planes to the observation plane are scaled as

$$\begin{aligned}h_{10}(x_0-u'',y_0-v'')&=h_{10}\left[m_T\left(\frac{x_0-u''}{m_T}\right),m_T\left(\frac{y_0-v''}{m_T}\right)\right]\\&=h'_{10}\left[\frac{x_0-u''}{m_T},\frac{y_0-v''}{m_T}\right]\\h_{20}(x_0-u',y_0-v')&=h'_{20}\left[\frac{x_0-u'}{m_T},\frac{y_0-v'}{m_T}\right]\end{aligned} \qquad \text{(A.17)}$$

Then, use of the substitutions

$$\begin{aligned}s_x&=\frac{u''}{m_T}-u\\s_y&=\frac{v''}{m_T}-v\\q_x&=\frac{x_0}{m_T}-u\\q_y&=\frac{y_0}{m_T}-v\end{aligned} \qquad \text{(A.18)}$$

yield the simple convolution of the point spread functions of the illumination and imaging portions of the test path (1), such that

$$\int_{-\infty}^{\infty}\int_{-\infty}^{\infty} h_{i1}\left(s_x, s_y\right) h'_{10}\left(q_x - s_x, q_y - s_y\right) ds_x ds_y \,. \tag{A.19}$$

Equation (A.19) is a function of $\left(q_x, q_y\right)$, which are the differences between the source coordinate and the observation-plane coordinate. When integrated over the source coordinates, the result is only a function of the observation-plane location.

Expanding Eq. (A.19) into the Fourier domain leads considerable insight into this problem. When the expansion is substituted back into Eq. (A.16), the result is

$$J_{12}\left(x_0, y_0\right) = \kappa \int_{-\infty}^{\infty}\int_{-\infty}^{\infty} M\left(\frac{x_0/m_T - q_x}{m_{Ti}}, \frac{y_0/m_T - q_y}{m_{Ti}}\right) h_{T_1}\left(q_x, q_y\right) h^*_{T_2}\left(q_x, q_y\right) dq_x dq_y \;, \tag{A.20}$$

where

$$h_{T_1}\left(q_x, q_y\right) = \mathbf{F}^{-1}_{q_x}\mathbf{F}^{-1}_{q_y}\left\{T'\left(\xi,\eta\right)\exp j2\pi\left[W_{T_1}\left(\xi,\eta\right)\right]\right\} \,, \tag{A.21}$$

$$h_{T_2}\left(q_x, q_y\right) = \mathbf{F}^{-1}_{q_x}\mathbf{F}^{-1}_{q_y}\left\{T'\left(\xi,\eta\right)\exp j2\pi\left[W_{T_2}\left(\xi,\eta\right)\right]\right\} \,, \tag{A.22}$$

$$T'\left(\xi,\eta\right) = \frac{1}{\left|m_T\right|^2} T_1\left(\xi,\eta\right) T_i\left(m_{Ti}\xi, m_{Ti}\eta\right) \,, \tag{A.23}$$

$$W_{T_1}\left(\xi,\eta\right) = W_1\left(\frac{\xi}{m_T}, \frac{\eta}{m_T}\right) + W_{i1}\left(\xi,\eta\right) \tag{A.24}$$

and

$$W_{T_2}\left(\xi,\eta\right) = W_2\left(\frac{\xi}{m_T}, \frac{\eta}{m_T}\right) + W_{i2}\left(\xi,\eta\right) . \tag{A.25}$$

From Eq. (A.23) to Eq. (A.25), the pupil functions from test and reference planes to the observation plane are also scaled due to the scaled coherent point spread function in Eq. (A.17).

In essence, $h_{T_1}\left(q_x, q_y\right)$ and $h_{T_2}\left(q_x, q_y\right)$ are the combined point spread functions of the illumination (subscript *i*) and imaging portions of the test path (1) and reference path (2), respectively, of the interferometer. $T'\left(\xi,\eta\right)$ is the effective limiting aperture of the system. $W_{T_1}\left(\xi,\eta\right)$ and $W_{T_2}\left(\xi,\eta\right)$ are the combined aberration functions of the illumination and imaging portions of the test path (1) and reference path (2), respectively.

Equation (A.20) can be simplified if we assume that the source is uniform, the aberrations are small and that the observation is made in the uniform region. Under these assumptions, Eq. (A.20) simplifies to

$$J_{12} \propto \int_{-\infty}^{\infty}\int_{-\infty}^{\infty} h_{T_1}\left(q_x, q_y\right) h_{T_2}^{*}\left(q_x, q_y\right) dq_x dq_y \quad , \tag{A.26}$$

which is simply overlap of the total coherent point spread functions from the test path (1) and reference path (2). J_{12} is not a function of $\left(x_0, y_0\right)$ in this region of the observation plane, so visibility is uniform.

Equation (A.26) is conceptually appealing. Maximum visibility is achieved with low or matching aberrations in each path. Displacements caused by alignment errors shift the point spread functions with respect to each other, so the overlap integral decreases rapidly. Defocus differences between the two paths cause one point spread function to be large compared to the other, and as such reduces the overlap. These conditions are illustrated in Fig. 3 of the July 25, 2008, report.

A.4 Kohler illumination

Consider a condenser that collimates a quasimonochromatic extended source, as shown in Fig. 2 of the July 25, 2008, report. The mutual intensity in the illumination pupil can be described by propagating from the source plane, through the condenser lens and to the illumination pupil. For the case where the illumination pupil is apart from condenser by a distance equal to the focal length of the condenser, the mutual intensity is[9]

$$J_i\left(x_i, y_i, x_i', y_i'\right) = \frac{1}{\left(\lambda f_C\right)^2} \int_{-\infty}^{\infty}\int_{-\infty}^{\infty}\int_{-\infty}^{\infty}\int_{-\infty}^{\infty} J_s\left(x_s, y_s, x_s', y_s'\right) e^{j\frac{2\pi}{\lambda f_C}\left(x_s' x_i' + y_s' y' - x_s x_i - y_s y_i\right)} dx_s dy_s dx_s' dy_s' , \tag{A.27}$$

where

$$J_s\left(x_s, y_s, x_s', y_s'\right) = \kappa M\left(x_s, y_s\right) \delta\left(x_s - x_s', y_s - y_s'\right). \tag{A.28}$$

In Eq. (A.27), it is assumed that the condenser is large enough to ignore its pupil function and there is no aberration. Substitution of Eq. (A.28) into Eq. (A.27) yields

$$\begin{aligned} J_i\left(\delta x_i, \delta y_i\right) &= \frac{\kappa}{\left(\lambda f_C\right)^2} \int_{-\infty}^{\infty}\int_{-\infty}^{\infty} M\left(x_s, y_s\right) e^{j\frac{2\pi}{\lambda f_C}\left[x_s \delta x_i + y_s \delta y_i\right]} dx_s dy_s \\ &= \frac{\kappa}{\left(\lambda f_C\right)^2} \mathrm{F}^{-1}_{\frac{\delta y_i}{\lambda f_C}} \mathrm{F}^{-1}_{\frac{\delta x_i}{\lambda f_C}} \left[M\left(x_s, y_s\right)\right] \quad , \end{aligned} \tag{A.29}$$

where $\delta x_i = x_i' - x_i$ and $\delta y_i = y_i' - y_i$. The effective mutual intensity of the reference and test planes is

$$J_{z_{12}=0}(x_1, y_1, x_2, y_2) = \frac{1}{|m_{Ti}|^2} \int_{-\infty}^{\infty}\int_{-\infty}^{\infty}\int_{-\infty}^{\infty}\int_{-\infty}^{\infty} J_i\left(\frac{u'-u}{m_{Ti}}, \frac{v'-v}{m_{Ti}}\right) \times h_{i1}\left(x_1 - u, y_1 - v\right) h_{i2}^*\left(x_2 - u', y_2 - v'\right) dudvdu'dv' . \tag{A.30}$$

From Eq. (A.24) of the July 25, 2008 report and Eq. (A.29), Eq. (A.30) becomes

$$\begin{aligned} J_{z_{12}=0}(x_1, y_1, x_2, y_2) = \frac{\kappa}{|m_{Ti}|^2 \left(\lambda f_C\right)^2} \int_{-\infty}^{\infty}\int_{-\infty}^{\infty}\int_{-\infty}^{\infty}\int_{-\infty}^{\infty} & \left\{ \int_{-\infty}^{\infty}\int_{-\infty}^{\infty} M\left(x_s, y_s\right) e^{j\frac{2\pi}{\lambda f_C}\left[x_s \frac{s_x}{m_{Ti}} + y_s \frac{s_y}{m_{Ti}}\right]} dx_s dy_s \right. \\ & \times \int_{-\infty}^{\infty}\int_{-\infty}^{\infty} T_i\left(m_{Ti}\xi', m_{Ti}\eta'\right) e^{j2\pi W_{1i}(\xi',\eta')} e^{j2\pi\left[\xi'(x_1-u)+\eta'(y_1-v)\right]} d\xi' d\eta' \\ & \left. \times \int_{-\infty}^{\infty}\int_{-\infty}^{\infty} T_i^*\left(m_{Ti}\xi'', m_{Ti}\eta''\right) e^{-j2\pi W_{2i}(\xi'',\eta'')} e^{-j2\pi\left[\xi''(x_2-s_x-u)+\eta''(y_2-s_y-v)\right]} d\xi'' d\eta'' \right\} dudvds_x ds_y , \end{aligned} \tag{A.31}$$

where

$$\begin{aligned} s_x &= u' - u \\ s_y &= v' - v \end{aligned} \tag{A.32}$$

Equation (A.31) can be reorganized as

$$\begin{aligned} J_{z_{12}=0}(x_1, y_1, x_2, y_2) = \frac{\kappa}{|m_{Ti}|^2 \left(\lambda f_C\right)^2} & \int_{-\infty}^{\infty}\int_{-\infty}^{\infty} M\left(x_s, y_s\right) \\ & \times \int_{-\infty}^{\infty}\int_{-\infty}^{\infty}\int_{-\infty}^{\infty}\int_{-\infty}^{\infty} \left\{ T_i\left(m_{Ti}\xi', m_{Ti}\eta'\right) T_i^*\left(m_{Ti}\xi'', m_{Ti}\eta''\right) \right. \\ & \times e^{j2\pi\left[W_{1i}(\xi',\eta') - W_{2i}(\xi'',\eta'')\right]} e^{j2\pi\left[\xi' x_1 - \xi'' x_2 + \eta' y_1 - \eta'' y_2\right]} \\ & \times \int_{-\infty}^{\infty}\int_{-\infty}^{\infty} e^{j2\pi\left[\left(\xi'' + \frac{x_s}{m_{Ti}\lambda f_C}\right)s_x + \left(\eta'' + \frac{y_s}{m_{Ti}\lambda f_C}\right)s_y\right]} ds_x ds_y \\ & \left. \times \int_{-\infty}^{\infty}\int_{-\infty}^{\infty} e^{j2\pi\left[(\xi''-\xi')u + (\eta''-\eta')v\right]} dudv \right\} d\xi' d\eta' d\xi'' d\eta'' dx_s dy_s \quad . \end{aligned} \tag{A.33}$$

Integrations with s_x , s_y , u and v yield delta functions. Using the sifting property of delta functions, Eq. (A.33) is simplified to

$$J_{z_{12}=0}(\delta x,\delta y)$$
$$=\frac{\kappa}{\left|m_{Ti}\right|^2}\int_{-\infty}^{\infty}\int_{-\infty}^{\infty}M\left(\lambda f_C u,\lambda f_C v\right)\left|T_i\left(-u,-v\right)\right|^2 e^{j2\pi\left[W_{1i}\left(-\frac{u}{m_{Ti}},-\frac{v}{m_{Ti}}\right)-W_{2i}\left(-\frac{u}{m_{Ti}},-\frac{v}{m_{Ti}}\right)\right]}e^{i2\pi\left[\frac{u}{m_{Ti}}\delta x+\frac{v}{m_{Ti}}\delta y\right]}dudv, \quad \text{(A.34)}$$

where $\delta x = x_2 - x_1, \delta y = y_2 - y_1$, $u=\frac{x_s}{\lambda f_C}$ and $v=\frac{y_s}{\lambda f_C}$. Notice that the effective mutual intensity in Eq. (A.34) is a function of coordinate differences δx and δy . From Eq. (10) ,

$$J_{12}\left(x_0,y_0\right)$$
$$=\frac{1}{\left|m_T\right|^2}\int_{-\infty}^{\infty}\int_{-\infty}^{\infty}\int_{-\infty}^{\infty}\int_{-\infty}^{\infty}J_{z_{12}=0}\left(\frac{u'-u}{m_T},\frac{v'-v}{m_T}\right)h_{10}\left(x_0-u,y_0-v\right)h_{20}^*\left(x_0-u',y_0-v'\right)dudvdu'dv'. \quad \text{(A.35)}$$

The mathematical procedure for continuing analysis of Eq. (B.35) is similar to the procedure used from Eqs (B.30) to (B.34). The result is

$$J_{12}=\frac{\kappa}{\left|m_T m_{Ti}\right|^2}\int_{-\infty}^{\infty}\int_{-\infty}^{\infty}M\left(\lambda f_C u,\lambda f_C v\right)\left|T_i\left(-u,-v\right)\right|^2\left|T\left(-\frac{u}{m_{Ti}},-\frac{v}{m_{Ti}}\right)\right|^2 e^{j2\pi W_T(u,v)}dudv \quad ,\text{(A.36)}$$

where

$$\begin{aligned}W_T\left(u,v\right)=&W_{1i}\left(-\frac{u}{m_{Ti}},-\frac{v}{m_{Ti}}\right)-W_{2i}\left(-\frac{u}{m_{Ti}},-\frac{v}{m_{Ti}}\right)\\&+W_1\left(-\frac{u}{m_T m_{Ti}},-\frac{v}{m_T m_{Ti}}\right)-W_2\left(-\frac{u}{m_T m_{Ti}},-\frac{v}{m_T m_{Ti}}\right)\end{aligned}. \quad \text{(A.37)}$$

Because of the same coordinates of the detector plane in Eq. (A.35), Eq. (A.36) doesn’t show Fourier transform relation.

DISTRIBUTION

1	MS0346	Daniel Rader	01513	
1	MS0372	James Redmond	01525	
1	MS0886	Paul Kotula	01652	
1	MS0886	Joseph Michael	01822	
1	MS1070	Channy Wong	01526	
1	MS1304	John Sullivan	01132	
1	MS1314	Jianyu Huang	01132	
1	MS0899	Technical Library	09536	(electronic copy)
1	MS0123	D. Chavez, LDRD Office	1011	

Sandia National Laboratories